VŠB – Technická univerzita Ostrava

Univerzitní studijní programy

Deposition and characterization of Y-substituted BIG thin films

Příprava a charakterizace Y dopovaných BIG tenkých vrstev

Author: Bc. Šárka Kunčická

Supervisor: doc. Dr. Mgr. Kamil Postava

Ostrava 2016

VŠB - Technical University of Ostrava
University Study Programmes
CNT - Nanotechnology Centre

Diploma Thesis Assignment

Student: **Bc. Šárka Kunčická**

Study Programme: N3942 Nanotechnology

Study Branch: 3942T001 Nanotechnology

Title: Deposition and characterization of Y-substituted BIG thin films
Příprava a charakterizace Y dopovaných BIG tenkých vrstev

The thesis language: English

Description:

Yttrium and Bismuth-substituted Iron Garnet (BIG:Y) exhibits gigantic magneto-optical effect and it is promising material for magneto-optical applications. Main target is preparation and characterization of series of thin-film samples using pulsed laser deposition on Gallium-Gadolinium Garnet (GGG). Samples are prepared in collaboration with GEMaC laboratory, University of Versailles. The main goals of the thesis are summarized in the following items:

1. Preparation of sample series of Y-substituted BIG layers by pulsed laser deposition.
2. Characterization of the deposition process by SEM target analysis and emission spectroscopy analysis of plasma.
3. Structural characterization of deposited layers (XRD, RHEED, AFM).
4. Magneto-optical and ellipsometric spectroscopy of prepared films, study of magnetic properties using magneto-optical techniques.

References:

B. Vertruyen, R. Cloots, J. S. Abell, T. J. Jackson, R. C. Da Silva, E. Popova, and N. Keller. Curie temperature, exchange integrals, and magneto-optical properties in off-stoichiometric bismuth iron garnet epitaxial films. Physical Review B 78, 2008, 094429.

E. P. Wohlfarth. Ferromagnetic materials: A handbook on the properties of magnetically ordered substances. Repr. Amsterdam: North-Holland, 1982.

S. Visnovsky. Optics in Magnetic Multilayers and Nanostructures, CRC Taylor&Francis, 2006.

B. D. Cullity and C. D. Graham. Introduction to Magnetic Materials, 2nd Ed. IEEE Press, 2009.

Extent and terms of a thesis are specified in directions for its elaboration that are opened to the public on the web sites of the faculty.

Supervisor: **doc. Dr. Mgr. Kamil Postava**

Date of issue: 20. 10. 2015

Date of submission: 16. 05. 2016

prof. Ing. Jaromír Pištora, CSc.
Head of Department

prof. Ing. Petr Noskievič, CSc.
Vice-rector for Study Affairs

Declaration

I declare I have elaborated this thesis by myself. All literary references and publications I have used had been cited.

Ostrava, May 16, 2016 .....

Šárka Kunčická

Prohlášení

- Byla jsem seznámena s tím, že na moji bakalářskou práci se plně vztahuje zákon č.121/2000 Sb. – autorský zákon, zejména § 35 – využití díla v rámci občanských a náboženských obřadů, v rámci školních představení a využití díla školního a § 60 – školní dílo.
- Beru na vědomí, že Vysoká škola báňská – Technická univerzita Ostrava (dále jen VŠB-TUO) má právo nevýdělečně, ke své vnitřní potřebě, bakalářskou práci užít (§ 35 odst. 3).
- Souhlasím s tím, že jeden výtisk bakalářské práce bude uložen v Ústřední knihovně VŠB-TUO k prezenčnímu nahlédnutí a jeden výtisk bude uložen u vedoucího bakalářské práce. Souhlasím s tím, že údaje o bakalářské práci, obsažené v Záznamu o zveřejněné práci, umístěném v příloze mé bakalářské práce, budou zveřejněny v informačním systému VŠB-TUO.
- Bylo sjednáno, že s VŠB-TUO, v případě zájmu z její strany, uzavřu licenční smlouvu s oprávněním užít dílo v rozsahu § 12 odst. 4 autorského zákona.
- Bylo sjednáno, že užít své dílo – bakalářskou práci nebo poskytnout licenci k jejímu využití mohu jen se souhlasem VŠB-TUO, která je oprávněna v takovém případě ode mne požadovat přiměřený příspěvek na úhradu nákladů, které byly VŠB-TUO na vytvoření díla vynaloženy (až do jejich skutečné výše).
- Beru na vědomí, že odevzdáním své práce souhlasím se zveřejněním své práce podle zákona č. 111/1998 Sb., o vysokých školách a o změně a doplnění dalších zákonů (zákon o vysokých školách), ve znění pozdějších předpisů, bez ohledu na výsledek její obhajoby.

V Ostravě 16. 5. 2016

Šárka Kunčická

Adresa trvalého pobytu: Hlavní třída 564, Ostrava – Poruba, 708 00

Acknowledgement

I would like to thank to my supervisor doc. Dr. Mgr. Kamil Postava for his guidance, motivation, inspirational ideas, will and finally his admirable patience during a troubleshooting with the organization of the thesis and programming.

Then, I would like to express my deep gratitude to Dr. Olena Popova and Dr. Niels Keller from the University of Versailles and the French National Centre for Scientific Research for their supervision during my internship in France. I am thankful for their comments, help when needed, and finally the possibility of holding the internship. They enabled me to learn as much as possible during the stay, showed how the scientific laboratory works, and how to conduct the research project.

Last but not least, I would like to thank Christéle Vilar for SEM measurements and Bruno Berini for guiding me through AFM measurements in Versailles, and Lukáš Halagačka for his advice regarding MO ellipsometric measurements in Ostrava.

ABSTRAKT

Granáty jsou nejvhodnějšími materiály pro magnetické a magneto-optické aplikace díky jejich velké magneto-optické odezvě a velmi dobrým magnetickým vlastnostem. Jsou transparentní a magneto-opticky aktivní ve viditelné a blízké infračervené oblasti (cca od 390 po 2500 nm). Tato práce ukazuje cestu celého experimentu od přípravy terče, přes proces depozice tenké vrstvy a její charakzterizace, až po konečné stanovení vlastností. Zaměřuje se na zkoumání možností dopování granátů a podmínek depozice tenkých vrstev, aby bylo dosaženo nejlepších magneto-optických vlastnosti. Většina experimentální práce je prováděna ve spolupráci s University of Versailles ve Francii. Dvě série krystalických Bi:YIG tenkých vrstev ($Bi_2YFe_5O_{12}$ a $BiY_2Fe_5O_{12}$) jsou připraveny na gadoliniovo-galliovo granátovém (GGG) substrátu pulzní laserovou depozicí (PLD) za změny tlaku O_2 a teploty substrátu. Charakterizační metody jako SEM, emisní spektroskopie, AFM, XRD, RHEED, profilometrie, elipsometrie a magneto-optika dohromady poskytují informace o morfologii tenkých vrstev, stechiometrii, chemickém složení, a krystalizaci, optických a magneto-optických vlastnostech.

Klíčová slova: Granát; Bi; Y; Bi:YIG; $Bi_2YFe_5O_{12}$; $BiY_2Fe_5O_{12}$; tenké vrstvy; GMR; depozice; PLD; GGG; charakterizace; SEM; emisní spektroskopie; AFM; XRD; RHEED; profilometrie; magneto-optika; spektroskopická elipsometrie; magneto-optický Kerrův jev; MOKE; Faradayův jev; MO spectra; longitudinální komponenta magnetizace; magnetometrie

Bibliografická citace:

KUNČICKÁ, Šárka, *Příprava a charakterizace Y dopovaných BIG tenkých vrstev.* Ostrava, 2016, 86s. Diplomová práce, Vysoká škola báňská – Technická univerzita Ostrava.

ABSTRACT

Garnets are the most suitable materials for magnetic and magneto-optical applications due to their large magneto-optical response and very good magnetic properties. They are transparent and magneto-optically active in a visible and near-infrared range (about 390 – 2500 nm). This thesis shows the procedure of the whole experiment from a preparation of a target, throughout a process of deposition of a thin film and its characterization, to final determination of its properties. The focus is laid on examining possibilities of doping garnets and thin film deposition conditions in order to obtain the best magneto-optical properties. Most of the experimental work has been done in a cooperation with the University of Versailles in France. Two series of crystalline Bi:YIG thin films (Bi2YFe5O12 and BiY2Fe5O12) have been prepared on gadolinium-gallium garnet (GGG) substrate by the pulsed laser deposition (PLD) varying O_2 pressure and substrate temperature. Characterization methods such as SEM, emission spectroscopy, AFM, XRD, RHEED, profilometry, ellipsometry, and magneto-optics altogether give information about thin films' morphology, stoichiometry, chemical composition, as well as crystallization, optical and magneto-optical properties.

Key words: Garnet; Bi; Y; Bi:YIG; $Bi_2YFe_5O_{12}$; $BiY_2Fe_5O_{12}$; thin film; GMR; deposition; PLD; GGG; characterization; SEM; emission spectroscopy; AFM; XRD; RHEED; profilometry; magneto-optical; spectroscopic ellipsometry; Kerr effect; MOKE; Faraday effect; MO spectra; longitudinal magnetic component; magnetometry

Reference format:

KUNČICKÁ, Šárka. *Deposition and characterization of Y-substituted BIG thin films*. Ostrava, 2016, 86p. Diploma thesis, VŠB – Technical University of Ostrava.

CONTENTS

1. INTRODUCTION

The garnets were extensively investigated and developed in the 1960s and 1970s during the creation of a nonvolatile computer memory and processor system based on moveable magnetized regions called bubble domains [1]. Recently, the magnetic garnets as magneto-optical transparent materials are extensively studied for novel applications in the area of telecommunications, integrated photonic circuits, and sensors. As today's requirements represent better sensitivity, compatibility with electronic systems, and smaller size of components for new magneto-optical devices, it is crucial to improve technology and materials.

Garnets (e.g. yttrium iron garnet (YIG), rare earth-garnet) have large magneto-optical response (Faraday and Kerr effect) and very good magnetic properties in general, so they are the most suitable materials for magnetic and magneto-optical applications. They are transparent and magneto-optically active in visible and near-infrared range (about 390 – 2500 nm). [2–4], which includes the wavelength usually used for optical telecommunications. YIG, bismuth iron garnets (BIG) or yttrium garnets substituted with bismuth oxide (Bi:YIG) can be used in magneto-optical devices, integrated optical circuits, blue semiconductor technology, photonics, spintronics, recording applications or microwave devices [1, 3, 5–8] Thin films of garnets usually manufactured by Pulsed Laser Deposition (PLD) or radiofrequency (RF) sputtering techniques are used in light control devices such as switches, deflectors, one-dimensional magneto-photonic crystals, circulators, reciprocal systems, or non-reciprocal parts in optical isolators [1, 4, 9, 10]. Nowadays, mainly bulk materials are used for these applications.

Therefore, an investigation of magneto-optical thin films or coatings has gained considerable interest. [11, 12] With the development of smart, low-power consumption devices comes a question of an energy conversion by means of converting a heat produced during an operation of the device into power required for its function. Combining Bi:YIG thin films with platinum coating represents significant part of spintronic research by transforming waste heat into electricity [13]. Combination of Bi:YIG thin films with Pt coating on the top can be used as nuclear-radiation detector detecting very small amount of gamma rays at a room temperature. Such detectors could replace the solid-state

detectors requiring cooling. [14] Pure YIG material is commonly used in microwave applications and as a detector of magnetic field [1, 11, 15–17]. In future applications, we will be probably able to find Bi:YIG garnets in the memory elements using spin-orbit coupling and magneto-electrical coupling, as this phenomena are currently studied.

Anyhow large is the range of application, it is important to meet certain conditions for large-scale production of such materials. The requirements include easy and reproducible deposition of thin films of a required quality with a specific value of refractive index (necessary for guiding of light), and appropriate magneto-optical properties. Though, the research in this field is necessary to broaden the knowledge and application use of garnets and to obtain information about possibilities of doping iron garnets with bismuth or yttrium.

In this thesis, I examine this possibilities of doping garnets together with the thin film deposition conditions in order to obtain the best magneto-optical properties because of the promising future application of Bi:YIG in magneto-optics. The motivation comes from the Erasmus stay internship in France lasting from May to July 2015 carried out between the Technical University of Ostrava and University of Versailles. Samples were prepared and characterized in collaboration with University of Versailles where the most of the experimental work took place at the laboratories of GEMaC (Group of Study of Condensed Matter) cooperating with CNRS (French National Centre for Scientific Research).

Chapter 1.1. describes the garnet material in detail. There is shown its crystal structure, origin of magneto-optical activity in garnets, and why the gadolinium gallium garnet substrate is the most suitable substrate for bismuth yttrium iron garnet thin films. In chapter 1.2., preparation methods of garnet thin films are summarized together with characterization techniques which goes hand in hand with the main properties observed in different scientific studies. Chapter 2 describes the pulsed laser deposition method (PLD) used for preparation of Bi:YIG thin films in this thesis. Chapter 3 presents an overview of methods used for characterization of thin films prepared during the internship in Versailles. Chapter 4 summarizes all the results obtained during the preparation of the Bi:YIG thin films and their characterization. There were prepared films of two series with compositions of $Bi_2YFe_5O_{12}$ and $BiY_2Fe_5O_{12}$. After that they were characterized by in-situ characterization techniques like Reflection High Electron Energy Diffraction (RHEED) to determine in-plane lattice parameter and to obtain the first information about the

crystallization of the sample, emission spectroscopy to determine chemical composition of the plasma during the deposition, and ellipsometry both, in-situ for measuring the thickness in the center of the sample, and ex-situ for determining optical constants and magneto-optical properties. Next ex-situ characterization techniques used were profilometry to measure the thickness on the edges of the samples, Scanning Electron Microscopy (SEM) to obtain a profile of element concentration across the target surface after the PLD deposition, Atomic Force Microscopy (AFM) to measure roughness and morphology, X-Ray Diffraction (XRD) to determine out-of-plane lattice parameter and presence of parasitic phases, and the last one, magneto-optical measurements of Kerr and Faraday effects to obtain information about magnetic properties and how they depend on stoichiometry of the samples (bismuth concentration).

1.1. Material's description

General crystal structure of a garnet forms a body centered cubic crystallographic lattice. Due to its crystal structure, iron garnet belongs to the centrosymmetric space group Ia3d [18]. It is very complex, and it contains eight formula units $A_3B_2C_3D_{12}$ in a unit cell for a total of 160 atoms (A = bismuth or yttrium, B and C = iron, D = oxygen). Those 160 ions are spread into four sites where 24 ions occupy the tetrahedral site, 24 ions occupy the dodecahedral site, 16 ions occupy the octahedral site, and 96 ions of oxygen from a neighborhood of the sublattices. Nevertheless, the primitive unit cell of garnet's crystal structure contains only 80 ions, 20 ions in each unit [18]. The iron garnet's structure is built-up of tetrahedra, octahedra and dodecahedra of metal cations coordinated with oxygen ions [7]. Figure 1 shows the structure of the garnet.

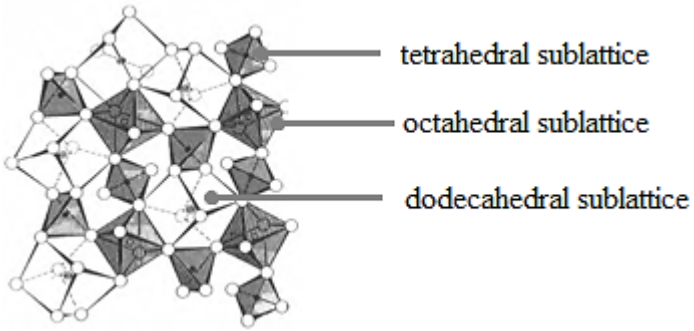

Fig. 1: Garnet crystal structure [19].

If we substitute pure yttrium iron garnet with bismuth or, for example, any lanthanide, it goes to the dodecahedral site and replaces some of yttrium atoms [19, 20]. Doping of bigger sized ions into the dodecahedral site can initiate a change in saturation magnetization of the garnets because the saturation magnetization of the garnet crystal is determined by the sublattice magnetization, and moreover is temperature dependent [18]. The total saturation magnetization of the garnets $M_s(T)$ can be written as a vector sum including all magnetization contributions:

$$M_s(T) = |M_t(T) \pm M_d(T) - M_o(T)|, \tag{1}$$

such as saturation magnetization of tetrahedral $M_t(T)$, dodecahedral $M_d(T)$, and octahedral site $M_o(T)$ [18].

The magnetization of octahedral and dodecahedral sublattices have the same direction, whereas the magnetization of tetrahedral sublattice is of the opposite direction. In iron garnets, the spontaneous magnetization arises from the contribution of magnetization of tetrahedral sublattice, when the tetrahedral site prevails over the octahedral site with a ratio of 3:2 [18]. Though, such decrease of magnetization can be caused by substituting magnetic ions into the lattice. It can occur for example when substituting bismuth atoms in pure BIG, where the direction of the magnetization was originally defined by tetrahedral sublattice. Then, other directions of magnetization of different sublattices can prevail. We can attain the magnetic compensation point when all magnetic contributions compensate each other and total magnetization turns into zero. It is possible to reach the compensation point by varying the temperature [4]. Figure 2 shows that garnet's magnetic properties originate from the antiparallel ordering between Fe^{3+} ions at octahedral and tetrahedral site which results from exchange coupling between the ions [21, 22].

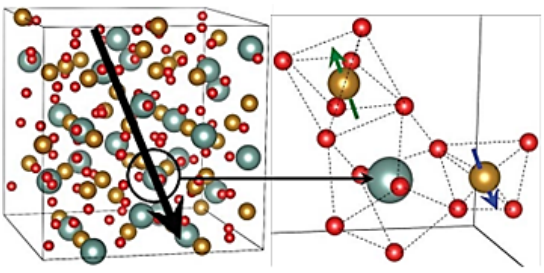

Fig. 2: Magnetic moment of the cell (black arrow) of a YIG crystal (left), and detailed view of contributing sublattices: spin-down tetrahedral and spin-up octahedral Fe^{3+} ions (golden) together with dodecahedral Y^{3+} ions (silver) forming a basis of the garnet structure [18].

Garnet thin films are commonly deposited on gadolinium gallium substrate (GGG). Gadolinium-gallium garnet (GGG – $Gd_3Ga_5O_{12}$) is a nonmagnetic material. Its lattice constant is of a nearest value to that of the garnet. Thus, GGG became one of the most suitable substrates for epitaxial growth of garnet thin films [4, 18, 23]. The lattice constant of $Gd_3Ga_5O_{12}$ crystal is 12.383 Å and the material is naturally paramagnetic and transparent in infrared range. It has got refractive index n = 1.95 at the wavelength of 1.06 μm. The lattice constant of Bi:YIG unit cell can climb up to 12.62 Å with a complete substitution of Bi [18].

Bismuth substituted yttrium iron garnet (Bi:YIG) belongs to a group of ferrimagnetic oxides (ferrites). It is a ferrimagnetic material due to its garnet structure. Ferrimagnetic materials have non-zero resultant magnetic moments. Hence, all unit cells form magnetic domain structures inside the iron garnet bulk material. By applying a strong magnetic field, all magnetic moments in garnet thin films can be aligned for MO activity (Fig. 3) [18].

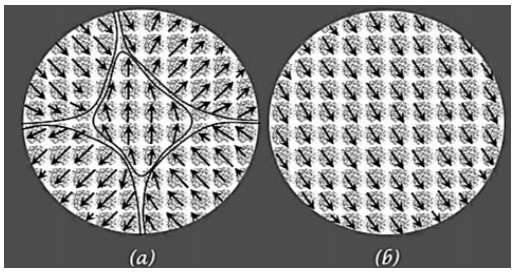

Fig. 3: a) Iron garnet's domain structures formed by a unit cell dipole moments, b) alignment of dipole magnetic moments by applied magnetic field [18].

Magneto-optical activity including Faraday rotation occurs in Bi:YIG when the off-diagonal elements of an electric permittivity tensor are non-zero. That occurs when orbital state for electric-dipole transition separates spectral energies for right- and left-handed circularly polarized planar waves. Splitting of the orbital angular momentum happens due to the spin-orbit coupling. For more information, see [18]. In Bi:YIG, Faraday rotation primarily results from the diamagnetic optical transition. It is also bigger in UV or visible light but smaller at far-IR frequencies. Absorption is present when the diagonal components of the tensor are complex. The Faraday rotation is also observed at near-IR

frequencies. All of these relations can be mathematically described by Kramers-Kronig relations.

1.2. Magneto-optical garnets and their properties

Bulk samples of pure bismuth iron garnets (BIG) are easier to produce than thin films of the same composition. In thin films of yttrium bismuth yttrium iron garnets, only several works have been done and it has been difficult to incorporate more than half of Bi atom to the structure with equilibrium growth techniques [21].

Bismuth iron garnets (BIG) and bismuth-yttrium iron garnets (Bi:YIG, Y:BIG) thin films are mostly grown by Pulsed Laser Deposition (PLD) [4, 5, 8, 10, 13, 14, 16, 20, 24], and they are usually deposited with thickness of several tens to a few hundreds of nanometers [4, 9, 13, 14, 24]. To obtain a high-quality garnet thin films with magneto-optical activity, the growth conditions and bismuth transfer from the target to the substrate need to be optimized. Depositions are performed with different oxygen pressure, substrate temperature, and varying the bismuth/iron content [6, 10, 20]. In many studies, Bi:YIG thin films were prepared by different **techniques**, such as PLD, dip coating, spin coating, Metal Organic Chemical Vapor Deposition (MOCVD) [16], radiofrequency (RF) magnetron sputtering [11, 16], Metal-Organic Decomposition method (MOD) [2, 25], Liquid Phase Epitaxy (LPE) [18], ion-bombardment [4], or Reactive Ion Beam Sputtering (RIBS) [26].

There can be prepared both polycrystalline [27] and mono-crystalline Bi:YIG thin films [18]. In following studies, they were grown on different **substrates**. Films prepared by PLD technique were mostly deposited on (111)-oriented gadolinium-gallium garnet (GGG – $Gd_3Ga_5O_{12}$) substrate in studies [5, 13, 16]. LPE grown mono-crystal layer of Bi:YIG was grown on (100)-oriented GGG substrate in [18]. Films prepared by MOD were deposited on amorphous glass substrate [2] and YIG thin films grown by RF magnetron non-reactive sputtering on quartz and (111)-GGG substrate [11].

In case of Bi:YIG thin films, similar **growth conditions** for the same deposition methods are used. In the study of Hayashi et al. epitaxial Bi:YIG thin film growth using PLD was achieved when the substrate temperature was about 500 °C and oxygen pressure between 125 –175 mTorr [10]. Crystallization of pure BIG film was achieved at a substrate temperature around 530 °C in the study of Popova et al. [6]. Other experimental results

shown that also RF magnetron sputtering provides good surface quality thin films during short crystallization and low temperature process [7, 28]. Thin films prepared by RF sputtering also shown better temperature stability than those prepared by PLD technique. YIG thin films most often prepared by RF magnetron sputtering were crystalized at the deposition temperature around 600 °C in [11]. Block et. al. fabricated Bi:YIG thin films by RF sputtering at temperature between 700 °C to 825 °C [28]. Bi:YIG thin films prepared by MOD method crystalized at temperature up to 750 °C [25]. Usually, the substrate temperature needed for the thin film to crystalize varies with bismuth and yttrium content in resulting sample and with oxygen pressure.

Thin films are usually characterized by various methods in order to discover properties related to their surface, morphology or crystal structure. In case of bismuth yttrium iron garnet thin films following **characterization methods** are used. In several studies, magneto-optical properties were usually investigated by *MO Kerr magnetometry* and *MO Kerr spectroscopy* [5, 6, 24]. Those methods represent valuable, cheap and nondestructive techniques for characterization of garnet thin films not thicker than 200 nm [24]. Results of the studies are usually explained using physical-mathematical models. When determining magnetic properties of Bi:YIG thin film, the conventional procedure is subtracting the substrate magnetization from the total magnetization of the sample [13]. An ellipsometric set-up, *Vibrating Sample Magnetometer (VSM)* or *compensation method* can be also used to determine MO properties [11, 26]. Optical properties (e.g. refractive index and optical absorption) of thin films are determined by *ellipsometry* [5, 28, 29]. Ellipsometry could be used to determine the thickness of the thin film, too. However, *profilometry* is used in most cases for this purpose [6, 11]. Another important characterization method is *X-Ray Diffraction*. (XRD). X-ray measurements are used to investigate crystallinity and presence of secondary phases in resulting thin films [11, 25, 27], as well as thin film's out-of-plane lattice parameter [4–6, 14]. Several microscopic techniques are used to characterize garnet thin films, too. *Atomic Force Microscopy (AFM)* and *Magnetic Force Microscopy (MFM)* measurements show morphology and magnetic structure of the sample surface [4, 6, 14]. The purpose of using *Scanning Electron Microscopy (SEM)* is to study chemical composition of thin films or targets [6]. *Reflection High Electron Energy Diffraction (RHEED)* helps to determine in-plane lattice parameter and whether the sample crystalized or not [4].

Several studies were performed to observe the magnetic and magneto-optical properties of BIG, YIG and Bi:YIG and showed that that their **properties** depend on thin film

composition and even more on deposition conditions [2, 4, 6, 8, 11, 16, 18, 26]. The influence of Bi/Fe ratio on thin film's properties was studied in [4], [6], and [11]. According to the studies in bulk garnets, it is expected that Curie temperature varies linearly with bismuth content (Fig. 4), and lattice parameter (Fig. 4), which has been proven by different authors [5, 7, 19, 20].

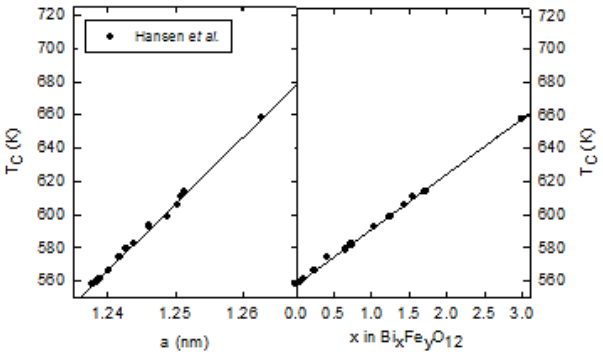

Fig. 4: Curie temperature as a function of a cubic cell parameter (a), and Bi content in the BIG thin film (x). The dashed line presents a linear fit to data measured in the study of Ventruyen et. al [20].

Together with Curie temperature the Faraday rotation varies, too [21, 23]. Garnets have in general high Curie temperature (T_C > 500 K) [23]. However, the value of Curie temperature for very thin garnet films can differ according to the composition. Ventruyen et al. studied the effect of stoichiometry on the structural, magnetic and magneto-optical properties of the bismuth iron garnet (BIG) thin films [20]. There were studied the effects of single iron sublattices – the octahedral and the tetrahedral one, and how their magneto-optical response changes. The scientists observed that the deficiency of bismuth affected the magneto-optical response of the tetrahedral iron sublattice, while small deficiency of iron affected more the magneto-optical response of the octahedral iron sublattice [20]. Ming-Yau Chern at al. measured the Faraday rotation spectra of Bi:YIG films [5]. Figure 5 shows Faraday rotation spectra with negative and positive Faraday rotations from 1.5 to 3.5 eV which came from the transitions in octahedral and tetrahedral Fe^{3+} ions with opposing spin magnetic moments in ferromagnetic garnet system [5].

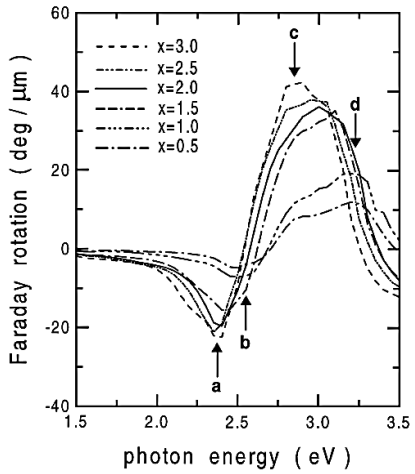

Fig. 5: Faraday rotation spectra of Bi:YIG films. Red shift is shown from b → a, and d → c for bismuth content (x) bigger than 1 [5].

Films with Bi content bigger than 1 showed a red shift in Faraday rotation curves probably caused by relaxation of Fe lattices. The shift assigned as a paramagnetic and diamagnetic transition was observed around 2.5 eV [5]. Lower Faraday rotation in Bi:YIG thin films may be the result of incomplete incorporation of Bi ions into the garnet lattice, or off-stoichiometry leading to the formation of iron ions with a valence state [27]. Researchers confirmed that MO properties dramatically increase with the amount of Bi content present in the film [7, 28]. The amorphous parts in the garnet film's volume could negatively influence Faraday rotation, too. Faraday rotation also vary with the thickness of the thin film and as a function of substrate surface conditions. Bi:YIG films prepared by conventional techniques like PLD often show perpendicular and easy-plane anisotropy, and has usually low saturation fields (up to 300 mT) which is often a disadvantage. [4] On the other hand, it is possible to use them in wide working temperature range up to 127 – 327 °C [16].

X-ray measurements in the study of Shaposhnikov et. al. determined the lattice parameter of Bi:YIG thin films to be about 12.602 Å for films prepared by PLD on GGG substrate with a number of Bi atoms per formula unit x = 2.8 [4]. The lattice parameter decreases as a function of increasing oxygen pressure [6]. Figure 6 shows high-resolution X-ray rocking curve obtained via XRD in the study of Ming-Yau Chern et al. [5].

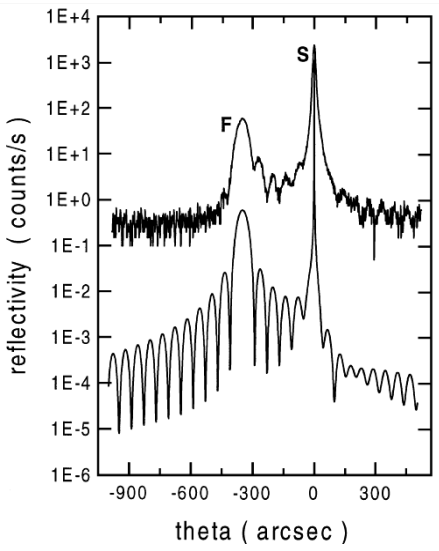

Fig. 6: High-resolution X-ray rocking curve of (444) reflections of $Bi_{0.5}Y_{2.5}Fe_5O_{12}$ film (F) on (111)-GGG substrate (S). Simulation of the rocking curve is shifted under the main curve [5].

In Figure 6, the high-resolution X-ray rocking curve was matched with the simulation and their similarity confirmed high crystalline quality of prepared Bi:YIG thin films [5]. Lee observed that secondary phases in Bi:YIG can originate from high substrate pre-annealing temperature and they strongly degrade the MO properties of measured thin films [25].

Another properties such as roughness, morphology, and its dependency on deposition conditions are studied using AFM. The roughness increases as a function of increasing oxygen pressure [6], and decreasing substrate temperature [16]. In the study of Shaposhnikov et al. the AFM measurements of morphology showed a single grains on the surface of the bismuth iron garnet thin film in the examined area (Fig. 7) [6].

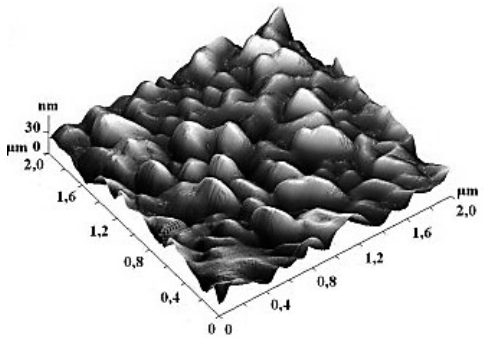

Fig 7: AFM image of the crystalized 112 nm BIG thick film [4].

Apparently, roughness of the thin films caused mainly by crystallites on the surface area is a normal phenomenon resulting from the deposition technique and conditions, and is most probably connected with high heating rates during the crystallization of the thin films [4]. It turned out that the grains does not affect magnetic properties of the thin films [6].

Ellipsometric measurements in the wavelength range from 260 nm (4.77 eV) to 1900 nm (0.65 eV) revealed that Bi substitution in YIG increases the refractive index in the low-energy spectral region and increases the absorption [23, 29]. Doormann et. al. studied optical and magneto-optical spectra of Bi:YIG thin films with Bi content of $0 < x < 1.42$ [29]. The refractive index and optical absorption measured by ellipsometry in [29] is shown in Figure 8.

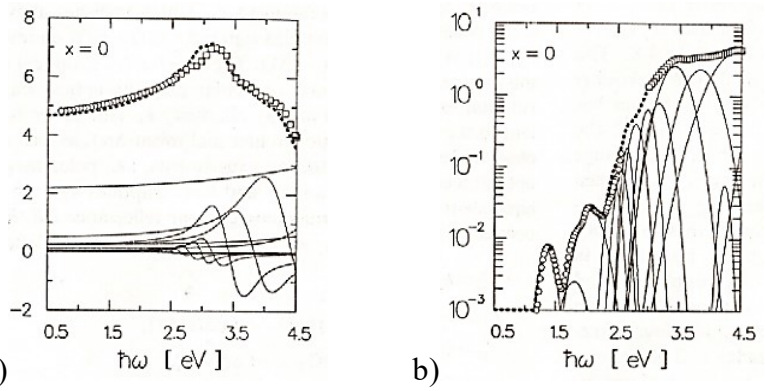

Fig.8: Optical spectra of real (a) and imaginary (b) part of the diagonal permittivity tensor component (ε_{11}) of Bi:YIG thin films obtained by ellipsometry [29].

MO properties in the same spectral range were obtained using phase modulated MO ellipsometry with photoelastic modulator (PEM). The spectra were fitted by Gaussian and by paramagnetic and diamagnetic line shapes and there was generated a table of coefficients of cubic polynomials which could be used for simulation of any measured spectra and any value of *x* [29].

Hayakawa et. al. reported that the atmosphere in which the thin films of Bi:YIG are prepared or annealed affected their optical properties [30].

2. PREPARATION OF BI:YIG THIN FILMS - PULSED LASER DEPOSITION (PLD) METHOD

Pulsed Laser Deposition (PLD) represents one of the physical vapor deposition methods (PVD). PLD technique creates stoichiometric thin films, however, yet in laboratory conditions. It usually creates fragile thin films but mostly of one phase compared to chemical vapor deposition methods (CVD). [31]

The aim of the PLD deposition process is to move the atoms from the heated source of the material (target) to the substrate which is located at some distance from the target, and which forms a layer. During the process, a high power laser ablates the material from the target into a vapor (the source atoms enter into the gas phase by physical mechanism). Chemical reactions are absent. The incident radiation is converted into thermal, chemical and mechanical energy and causes excitation of atoms of the target, ablation, surface exfoliation, and creates the plasma. The directional plasma plum contains of neutral atoms, molecules, ions, electrons, atomic clusters, micron size particles and molten droplets. [32] The high power laser is situated outside the deposition chamber and focused on the target by the set of external lenses. The deposition chamber contains windows for optical control of the deposition process. They must be transparent in the visible spectrum and must not absorb the laser radiation. Materials used are MgF_2, sapphire, CaF_2 and UV first-quality quartz. The deposition could be performed in vacuum or in gas atmosphere (e.g. oxygen). [32] Figure 9 shows the PLD setup.

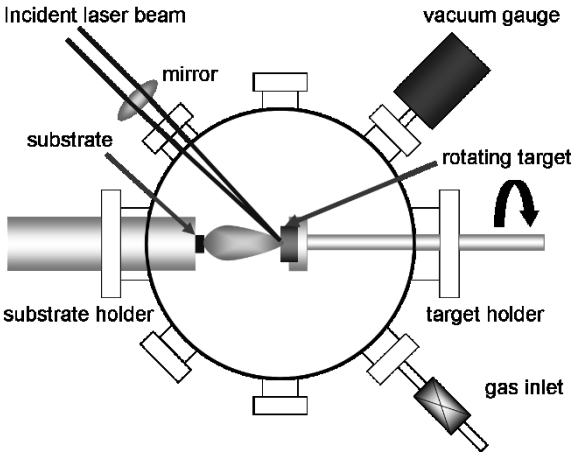

Fig. 9: Schematic of PLD setup for deposition of metal oxides [33].

PVD uses solid or molten sources. Solid targets for PLD, from which the layers are deposited, are created for example by sintering individual powders together to create film's desired composition [32]. For the purpose of this thesis, two targets with different compositions were prepared. The precursors BiO_3, Y_2O_3, and Fe_2O_3 were mixed in two different ratios (Bi/Y ratio) for each series (first series Bi_2YIG, second series BiY_2IG). After mixing the powders they were milled in a planetary ball mill with ZrO_2 grinding balls. This procedure was followed by pressing and sintering to obtain the targets.

PLD using a solid state Nd:YAG laser was used for all thin film depositions in this thesis, and the only conditions varied were substrate temperature during deposition and oxygen pressure in vacuum chamber (conditions with the biggest effect on stoichiometry)

The disadvantage of PLD the „splashing" of macroscopic particles on the substrate during the deposition. This can be eliminated e.g. by rapidly rotating pinwheel-like wheel that captures the slower moving, heavier particles [32]. General limitations of PVD techniques are difficulty in coating of large surfaces or components of a complex shape. The method is also quite costly because it needs sophisticated equipment (vacuum systems, reactor). The advantages are high deposition speeds, good vacuum, and clean environment for the deposition. It is also applicable to all types of materials.

3. CHARACTERISATION METHODS

3.1. Scanning Electron Microscopy (SEM)

SEM – Scanning Electron Microscopy – is a method that uses a moving electron beam to capture sample image. The main difference between an electron microscope and an optical microscope is that photons are replaced by electrons and glass lenses by electromagnetic lenses. Electromagnetic lenses (clutch) are represented by electromagnetic coils. The electron beam is deflected by a system of deflection coils and focused on the examined sample surface. Electromagnetic lenses may have defects, as well as optical lenses. A sources of accelerated electrons are usually tungsten filament or LaB_6 crystal, both of them being thermoemission sources, or FEG (field emission gun) – cold tungsten filament etched into the tip (high vacuum). [34]

The limit resolution is proportional to the wavelength of the radiation. Electrons have significantly shorter wavelength than visible light. Thus, the electron microscope has much higher resolution and it can achieve much higher effective magnification (up to 1 000 000x) than the light microscope. Therefore, the resolution of the electron microscope can be influence by the accelerating voltage, i.e. the voltage between the anode and the cathode [35]

Scanning electron microscopy is an indirect method of measurement. The sample image is formed by secondary electrons (SE - secondary electrons) emitted after the electron beam impinges on the sample surface. SE originate from inelastic collisions with electrons from the outer electron shells of atoms. This measurement mode provides information about the sample surface. Backscattered electrons (BSE) originate from elastic collisions with electrons from the outer electron shells of atoms. BSE mode provides information about the sample surface together with its chemical composition. Which electrons are emitted depends on the applied voltage. [36]

SEM works with vacuum. The vacuum chamber is equipped with a table on which the discs with the samples are placed. The table is movable in x, y, z axis, it can be tilted, and the position of the table is visualized by a CCD camera.

Specimens should not contain any foreign particles, charge itself, they should be stable in a vacuum and dry. The sample must be conductive to prevent charging and deformation of the specimen. Nonconductive specimens must be coated with electrically conductive layer (Au, Pt, and C) by vacuum deposition or ion sputtering. Biological samples must be dried [34].

The advantage of SEM is a large depth of field image, and thus its three-dimensional aspect. SEM can be used to extend database of conventional metallography, examine geological samples, analyze phases or minerals in rocks, but also to analyze the targets after the deposition of thin films to control its stoichiometry. Scanning electron microscope is capable of providing elemental spectra within the software and databases in the computer.

3.2. Atomic Emission Spectroscopy

Atomic Emission Spectroscopy (AES), also called an Optical Emission Spectroscopy (OES), examines the wavelengths of photons emitted by atoms and molecules as they transit

from a higher energy state to a lower one. Transitions in an atomic emission spectra are shown in Fig. 10.

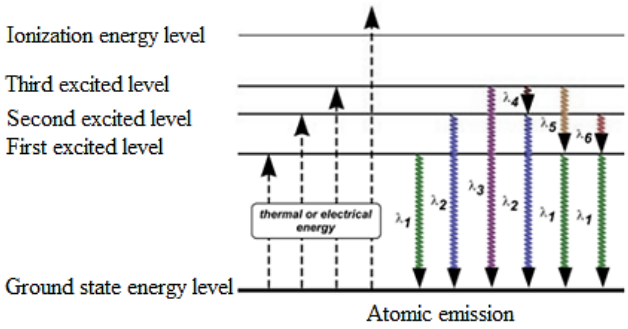

Fig. 10: Atomic transitions in an atomic emission spectra. Selection rules apply [37]

The method uses a quantitative measurement of optical emission of excited atoms to determine the concentration of elements in the sample or in plasma during the deposition process. In AES, the high temperature sources also cause the thermal (collisional) excitations. Usually, the higher temperature is, the more thermal excitations occur. For example laser pulses used as a source for our deposition provide sufficient energy to excite the atoms into higher energy levels.

Each element has got a characteristic set of wavelengths emitted depending on its electronic structure. Emission spectra of free atoms has a character of line spectra so they consist of very narrow peaks. Those occur for well defined, quantized electronic energy levels. The emission from elemental ions is measured, too. [38]

As an output, we get an emission spectra representing a dependence of intensity on wavelength, where the intensity (emission signal) is proportional to the population of the excited levels [38]. Thus, in our case, we are able to investigate stoichiometric transfer from the target to the sample by means of checking the amount of ablated elements in plasma which are deposited on the substrate in certain ratio. We are able to check whether there are not any other chemical compounds (e.g. oxides) which are not desired to be in the resulting film.

3.3. X-Ray Diffraction (XRD)

X-Ray Diffraction (XRD) analysis studies the fine structure of the material by means of diffraction of X-rays at the crystallographic lattice. Given that the wavelength of X-ray beams is similar to that of the interatomic distances in the crystals, this radiation is particularly suitable for examining the crystal structure of the materials.

XRD is the most widespread in the natural sciences and engineering thanks to the possibility of quantitative and qualitative analysis of crystalline substances, identification of the texture and crystal structures of unknown samples, determination of the size of crystals in polycrystalline materials, investigation of single crystals and determination the structures of crystalline phases, and structural analysis of organic compounds. [39] In thin film physics the X-Ray diffraction is used where accurate measurements of lattice parameters or phase analysis are required. XRD may be also used for the study of mechanical stresses in films. [36]

The method is based on the interaction of X-rays with electrons of atoms of analyzed material. The interaction is described by the fundamental equation – Bragg condition:

$$n \cdot \lambda = 2 \cdot d \cdot \sin\theta, \tag{2}$$

where θ is the diffraction angle (Bragg angle), d is the distance between crystallographic planes in the lattice, λ is the wavelength of the radiation used, and n is the order of diffraction. The X-ray beam is incident to two parallel crystallographic planes and scattered. Interference maximum (maximum intensity) of scattered waves occurs when the path difference (i.e., $2 \cdot d \cdot \sin\theta$) is equal to an integer multiple of the wavelength λ, or their phase difference is equal to an integer multiple of 2π. Bragg's condition therefore indicates the formation of the diffraction peaks.

A key device for X-ray diffraction analysis is the diffractometer. It consists of several parts. X-ray tube with a tungsten cathode and an anode from a metal plate (Cu, Mo, Fe, Co) are used as a source [39]. A high voltage is maintained between the anode and the cathode. The X-ray beam is coming out through beryllium windows. The detector can capture x-ray radiation coming from the sample at different angles. The diffraction angles are much greater for X-Rays, enabling to determine the lattice parameters with much higher precision, than with electron diffraction. [36] Nowadays, the most common detectors are scintillation, semiconductor, or synchrotron detectors [39]. The detectors have a certain sensitivity so they

can be destructed by too intense X-ray radiation scattered from the sample (i.e. when measuring an unknown sample). We can avoid that using filters (kβ-Ni plate, Cu, or Al plate). Screens and filters regulate the conditions of measurement for the selected sample and adjust the incident beam. Generally, we can analyze solid, single crystal or powder samples. The powder samples are usually compressed into tablets and have to be homogenized. Flat surfaces – thin films – provide the best results of the analysis. The diffraction pattern is produced by the whole thickness of the sample, or possibly even by the substrate. That can be helpful in determining the lattice constant of the material. We choose the sample holder according to its structure. The sample is rotated with respect to the X-ray tube. [39] Diffractometer is mostly controlled and programmed via a computer and appropriate software.

XRD is often compared with electron diffraction methods. In thin film physics electron diffraction is used more frequently than XRD. X-rays are more likely to penetrate deeper than electrons but their diffraction spots are about 10^3 times weaker. XRD is more suitable for thicker specimen, however, the diffraction pattern is obtainable also for very thin samples, down to 5 nm [36].

3.4. Reflection High Energy Electron Diffraction (RHEED)

Reflection High Energy Electron Diffraction (RHEED) is a technique used for studying the crystal structure, particularly for examination of the structure of the surface (thin film). Electrons from an electron gun reach the surface of thin film at a grazing angle, and the diffraction pattern can be observed on a screen [36]. The electron beam has an energy of 30 to 100 keV. Diffraction patterns depend on the quality of the surface. The more atomically smooth the surface is, the better the diffraction pattern appears. That means the appearance of parallel lines. For not such smooth surfaces, pronounces points appear instead of the lines, and for very rough surfaces, the diffraction pattern is made up of individual points. Another factor influencing the diffraction pattern look is the orientation of the specimen with respect to the incident beam. The apparatus is usually equipped with rotator of the specimen situated in vacuum (for example inside the deposition chamber) [36].

3.5. Atomic Force Microscopy (AFM)

Atomic Force Microscopy (AFM) belongs, together with scanning tunneling microscopy (STM), to one large group called the scanning probe microscopy (SPM). There are many techniques derived from SPM and more than 40 various measurement modes nowadays. Some of the techniques are LFM (Lateral Force Microscopy), MFM (Magnetic Force Microscopy), EFM (Electric Force Microscopy) or SCM (Scanning Capacitance Microscopy).

Atomic force microscopy shows only sample surface, not its volume structure. In comparison with optical microscopy, AFM achieves greater resolution, in order of nanometers. This resolution is comparable to that of an electron microscopy. The advantage of AFM is that it provides 3D images, whereas electron microscopy is only capable of 2D projection. There is no need of special treatment of the sample before measurement. The disadvantage is that the imaging of the sample could be quite slow and there is a limit in the range of the image size (up to hundreds of nm). There is only a limit of height of the sample that should not be higher than tents of micrometers.

Scanning probe microscopy could be divided into two basic measurement techniques. The probe moves either along and very close to the sample surface, or the probe remains stationary and the sample moves. Measuring probes for AFM are formed by a chip (base), and a cantilever with a tip. The most important parameters are the cantilever's stiffness and resonant frequency. AFM works in three basic modes, contact, semi-contact and non-contact mode. Basic characteristics of cantilevers for contact and semi-contact mode are following:

- The force F acting on the specimen surface is calculated by Hook's law: $F = k_n \cdot Dz$, where k_n is the stiffness of the cantilever, and Dz is the distance the lever is bent in the z axis.
- Contact mode: Arm stiffness $k_n \sim 0.1$ - 10 N / m, length $l \sim 100$ - 500 nm, resonant frequency $f \sim 1$ to 10 kHz.
- Non-contact mode: Arm stiffness $k_n \sim 10$ - 100 N / m, length $l \sim 10$ - 100 nm, the resonance frequency $f \sim$ 100-300 kHz [40].

The motion devices are called scanners and are mostly made of piezoelectric ceramics. The most common method of detecting the bending of the cantilever is optical detection of reflected laser beam by a quadrant light detector.

In contact mode, the tip is in contact with the sample due to the repulsive forces. Cantilever is less stiff than the bonding forces between atoms of the sample. Cantilever is deflected by the surface topography during scanning. Van der Walls' forces and electrostatic repulsion take place. In the contact mode, there is either a measurement mode with constant height where the cantilever's banding is detected, or with a constant force where the sample or the tip moves in the z direction.

In non-contact mode, called tapping, the cantilever is tapping over the surface of the sample and their distance is in the order of 1 - 10 nm. The amplitude is 1 nm and the vibrations have a frequency in the order of 100 - 400 kHz. The stiffness of the cantilever is important here because the tip is attracted to the sample and it must not be damaged.

Thus, the main difference between contact and non-contact mode is a requirement for the cantilever with the tip on its stiffness and resonance frequency. Next difference are the forces between the tip and the sample. When measuring, the force acting on the cantilever, the scanning speed, and the sensitivity of the feedback (detected using laser reflection) plays an important role.

AFM may also be used for examination of thin layers by measuring their roughness, thickness. It can be used for analysis of nanostructures, morphology and even the individual grains of the materials and their size.

3.6. Profilometry

Profilometry is one of the techniques determining the thickness of thin films. Thickness is one of the most important thin film parameters since it determines the properties of the film. Profilometry used for the purpose of thickness measurement for this thesis is often called the Stylus Method or Stylus Profilometry [36, 41]. Stylus, or contact, profilometry is the earliest form of profilometry.

The profilometer's main parts are a detector and a sample stage. The detector determines the position on the sample, and sample stage holds the sample. Both parts can be moveable. The stylus profilometer uses a probe (a diamond tip of a radius of 0.7 to 2 μm) to detect the surface of the sample. The probe is pressed onto the surface (usually with a pressure of 49 MPa) and physically moves along the selected area of the surface to acquire the surface height and roughness. Irregularities of the sample surface are recorded by converting the

movement of the probe registered by a feedback loop into an electrical signal which is then amplified. [36, 41] On the soft surface, the probe can be contaminated and the sensitivity is then limited. In certain cases, it may cause the destruction to the surface [41]. Though, the method is very suitable for thin films.

In case of our samples, the profilometry was used to measure the thickness on the edges of the thin film. For each sample, eight values were obtained and averaged. For each measurement, the error was calculated.

3.7. Spectroscopic Ellipsometry

An important technique used for measuring the optical and magneto-optical spectra is a spectroscopic Mueller matrix ellipsometry, which is optical measurement technique. It uses polarized light to measure optical properties of the materials, either by reflection, or transmission of light. It can be used to determine the optical functions of thin film or its thickness. The technique is called ellipsometry due to its origin in polarized light which becomes elliptically polarized after reflection of the linearly polarized light.

The polarization of light represents a cornerstone of spectroscopic ellipsometry. It describes a behavior of the wave´s electric field in a space and time. We speak about an unpolarized light if the oscillating direction of the light waves is random. According to the phase shift between the light waves, the polarization changes from linear to circular. Completely polarized light means that the relative phase between the different components of the electromagnetic field along two orthogonal directions remains constant. When the waves are 90° out of phase and have equal amplitude, the light is circularly polarized. The general elliptical polarization is a combination of the orthogonal waves of arbitrary amplitude and phase (Fig. 11). [42]

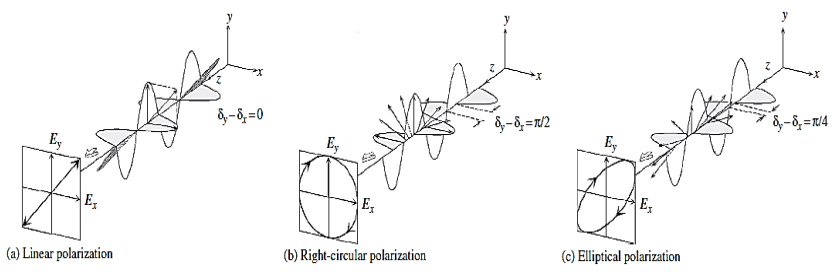

Fig. 11: Representations of (a) linear polarization, (b) circular polarization and (c) elliptical polarization [42].

The basis of ellipsometric measurement is an ellipsometer which usually combines high accuracy and precision. Spectroscopic Mueller matrix ellipsometry measurements are carried out in the wide spectral range from UV, visible to near-infrared region. The ellipsometer's important parts contain light source, polarization generator, and polarization sensitive detector. The detector can be realized for example by rotating analyzer containing rotating polarizer, rotating compensator, or phase modulator.

Measurements for the thin film samples prepared within this diploma thesis were performed on the VASE ellipsometer RC2-DI from J. A. Woollam Co., Inc. Corporation. The ellipsometer contains a dual rotating compensator and enables complete Mueller matrix characterization. It measures in a wide spectral range from 0.74 eV to 6.42 eV (wavelength region from 193 nm to 1700 nm). A software for enquiring and exporting all measured data is called Complete Ease and it was developed at the same company. Figure 12 shows a schematic illustration of the ellipsometric measurement.

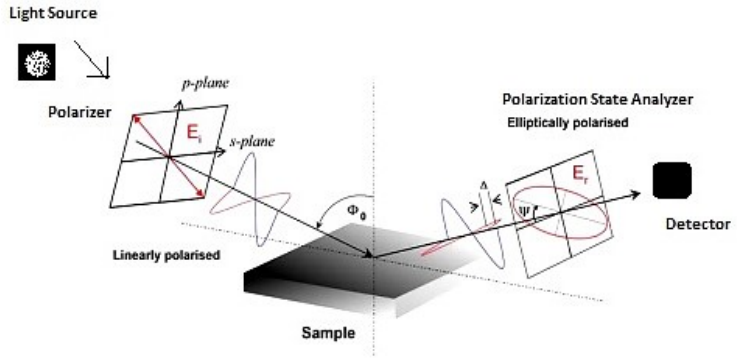

:

Fig. 12: A schematic illustration of the ellipsometric measurement: typical configuration. Incoming linearly polarized light with the azimuthal angle of 45° is reflected from the surface. The polarization change determining the response of the sample is measured. The light beam remains completely polarized during the classical ellipsometric measurement [42].

Data representing the polarization change are the ellipsometric angles Ψ and Δ. Their relation is given by the following equation:

$$\rho = \frac{r_p}{r_s} = \tan(\Psi)\, e^{-i\Delta}, \tag{3}$$

where Ψ represents a ratio of reflected s- and p- polarized waves, and Δ the phase difference of reflected s- and p- wave. The complex reflectance ratio ρ is given by the ratio of s- and p- polarized light. The spectra are measured simultaneously by multichannel CCD detector.

By Mueller matrix ellipsometry (Mueller Matrix Polarimetry), it is possible to measure the physical properties of partially polarized light and characterize anisotropic or depolarizing samples that are interesting for scientific research [42]. To get control of the principles of an ellipsometric measurement it is important to comprehend the Jones formalism and Stokes – Mueller formalism. These two formalisms are needed to describe the polarization of light mathematically. The optical and magneto-optical response of a material is based on Jones reflection and is described by reflection matrix:

$$R = \begin{bmatrix} r_{ss} & r_{ps}(M_P, M_L) \\ r_{sp}(M_P, M_L) & r_{pp}(M_T) \end{bmatrix}. \tag{4}$$

Magneto-optical Kerr effect for s- and p- polarization can be investigated on reflection as

$$\Phi_s = \tan(\Psi)_{sp}\, e^{-i\Delta_{sp}} = \frac{r_{sp}}{r_{ss}} = \theta_s + i\epsilon_s, \tag{5}$$

$$\Phi_p = \tan(\Psi)_{ps}\, e^{-i\Delta_{ps}} = \frac{r_{ps}}{r_{pp}} = \theta_p + i\epsilon_p, \tag{6}$$

where $\theta_{s,p}$ represents Kerr rotation and $\epsilon_{s,p}$ Kerr ellipticity. Optical permittivity of a material is given by

$$\varepsilon = \Re(\varepsilon) + i\Im(\varepsilon), \tag{7}$$

where imaginary part $\Im(\varepsilon)$ is given as arbitrary spectra for energies E_i ($\Im(\varepsilon_i)$), and real part $\Re(\varepsilon)$ is then calculated from Kramers-Kronig relations.

3.8. Magneto-optical effects

Magneto-optical effects were firstly discovered by M. Faraday in 1846 who was followed by J. Kerr in 1877. The MO effects occur when the polarization states of light are changed by the interaction with a magnetic material. Magnetic field causes the splitting of energy levels resulting in splitting of spectral emission lines. This phenomena is called the

Zeeman effect (1896) which can be found in to different configurations – longitudinal and transversal. The splitting of spectral lines is proportional to strength of the external magnetic field. In fact, MO effect originates from inner magnetic state of the substance defined by magnetization ***M.*** Zeeman effect stands behind the origin of MO effects due to its effect on the polarization of light. [43] According to the arrangement of the experiment, MO phenomena are divided into effects in transmission or reflection.

MO effect in reflection is called magneto-optical Kerr effect (MOKE). MOKE is measured at three different configurations: polar, longitudinal, and transversal, depending on the orientation of the magnetic field related to the sample surface and the plane of incidence of light (Fig. 13).

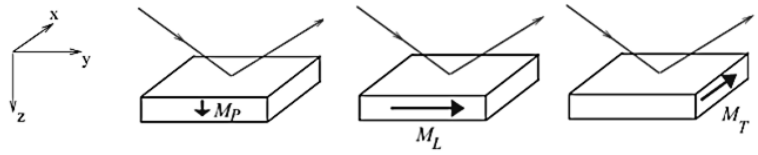

Fig. 13: Basic MOKE configurations – polar, longitudinal and transversal [44].

In polar MO Kerr effect (PMOKE), which is proportional to the out-of-plane magnetization component, the magnetization *M* is perpendicular to the sample surface Longitudinal MO Kerr effect (LMOKE) is observed when magnetization *M* lies in the plane of the sample surface and is parallel to the plane of incidence. In the third configuration, transversal MO Kerr effect (TMOKE) occur when magnetization *M* lies in the plane of the sample surface and is perpendicular to the plane of incidence. LMOKE and TMOKE are proportional to the in-plane magnetization components. [44] MOKE effect in a cubic crystal is described by the permittivity tensor:

$$\hat{\varepsilon} = \begin{bmatrix} \varepsilon_0 & -\varepsilon_1 m_z & \varepsilon_1 m_y \\ \varepsilon_1 m_z & \varepsilon_0 & -\varepsilon_1 m_x \\ -\varepsilon_1 m_y & \varepsilon_1 m_x & \varepsilon_0 \end{bmatrix}, \tag{8}$$

where MO signal is proportional to $\varepsilon_1(m_i)$, and magnetization directions m_x, m_y, m_z correspond to TMOKE, LMOKE and PMOKE respectively.

If we talk about the MO effects in transmission, we consider the relation between the direction of magnetization and the plane of incidence of light, too. One of the MO effects in transmission is Faraday effect. In Faraday geometry, the light propagates along the magnetic field. At this configuration, when linearly polarized light is rotated after passing through a material exposed to a magnetic field, the effect is called Faraday rotation – θ_F or magnetic circular birefringence (MCB) [12]. Linearly polarized light is actually composed of two different circularly polarized waves of opposite handedness (left and right). Consequently, when the linearly polarized light enters the material and changes its polarization into the elliptical one, the Faraday ellipticity – ϵ_F (magnetic circular dichroism) arises [21, 45]. Another case of MO effect in transmission is Cotton-Mouton effect (birefringence) that is observed in liquid media. Studying of Cotton-Mouton effect gives information about molecular structure and molecular mobility of the substance by rotating the anisotropic molecules along an external field. Cotton-Mouton effect behaves similarly to Voight effect. Both arise with the configuration of light propagating perpendicular to the magnetic field [43, 45]. MO effects in transmission are shown in Fig. 14.

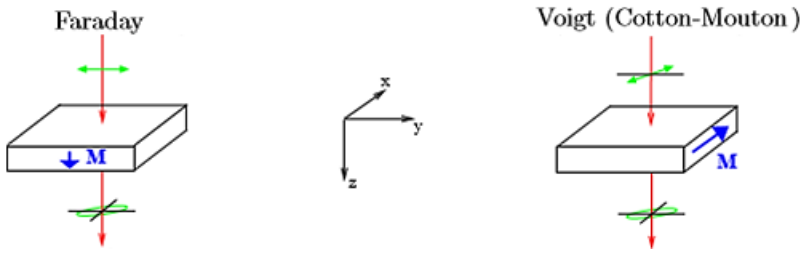

Fig. 14: Configurations of MO effects in transmission – Faraday effect, Voight (Cotton-Mouton) effect [43].

3.9. Magneto-optical measurements

MO hysteresis loop measurement is based on detection of MO signal which is proportional to the magnetization as a function of the external field.

Faraday rotation and Faraday ellipticity were measured at MO setup with polar configuration for all prepared samples. The applied external field was 10 000 Oe (1 T) and the wavelength of incident light was 550 nm.

The longitudinal Kerr effects were measured for two prepared samples at s- and p-polarization of incident light on laboratory magneto-optical set-up shown in Figure 15.

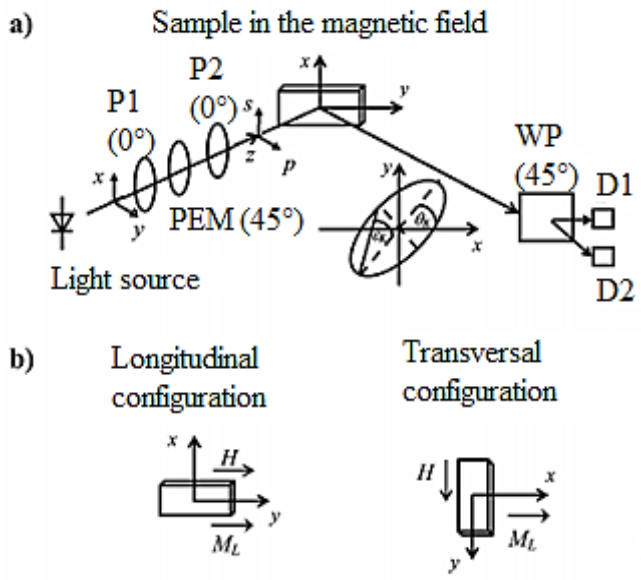

Fig. 15: a) A block diagram of a laboratory set-up – magneto-optical differential method used for measuring surface hysteresis loops. b) Longitudinal and transversal magneto-optical configuration for detecting a component parallel and perpendicular to the applied field using the longitudinal magneto-optical effect (longitudinal component of magnetization M_L) [46].

Hysteresis loops were measured by an experimental configuration using a differential intensity method – magneto-optical vector magnetometry – which measures all three components of the magnetization vector (polar, longitudinal, and transversal). A semiconductor red laser with the wavelength of 670 nm and power of 10 mW was used as a light source. Incident light beam was modulated at the frequency of 100 kHz using a photo-elastic modulator (PEM) inserted between two polarizers (P1 and P2), and linearly polarized light by the polarizer (P2) incident on the sample. We distinguish two basic polarization directions: s-polarization (perpendicular to the plane of incidence, transverse electric wave TE) or p-polarization (in the plane of incidence, a transverse magnetic wave TM). The incident angle $\alpha = 45°$ was used and the sample was placed in the center of quadrupole magnet creating external magnetic field of 223.8 Oe / A. The electric current is typically set to the value of 5 A. The polarization of light changed by the reflection from the sample to generally elliptical one and then passed through 45° rotated Wollaston prism (WP) dividing it into two mutually orthogonal linearly polarized beams. Those beams were detected by two silicon detectors (D1 and D2). It can be shown that the difference signal is directly

proportional to the MO Kerr rotation angle, or MO Kerr ellipticity angle if a quarter wave plate at the azimuth of 45° is inserted in front of the Wollaston prism. [46]

3.9.1. MOKE measurement procedure

The sample was rotated from 0° to 360° and measured at every 45°. For each position, the Kerr rotation and ellipticity were measured for the primary reflected laser beam (reflected from the top of the surface), and secondarily reflected laser beam (reflected from the backside of the substrate) (Fig. 16). Note that the secondary beam is rather double transition through Bi:YIG layer.

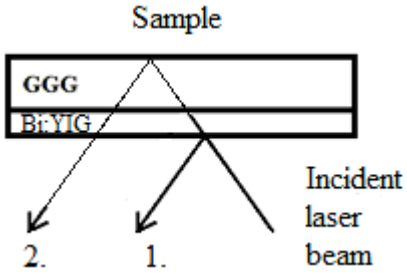

Fig. 16: Schematic of the measurement of MO effect – primary (1.) and secondary (2.) reflected laser beam.

The first and second reflections are showed below for each angle of rotation. After the measurement there were compared raw hysteresis loops of both, rotation and ellipticity, and their values of saturation magnetization. Then the longitudinal, polar and transversal effects were calculated for each configuration, i.e. numerical separation of contributions from different positions in the thin film was made.

3.9.2. Separation of magnetic components

For oblique incidence the Kerr rotation and ellipticity is the sum of the longitudinal (magnetization in the plane of incidence and in the film) and polar MO effect (magnetization perpendicular to the sample surface). Their separation is explained below on the basis of symmetry arguments [47] The in-plane magnetization perpendicular to the external field

(transversal component) is measured by the longitudinal Kerr effect by rotating sample and external magnetic field by 90 degrees as shown in Fig. 17.

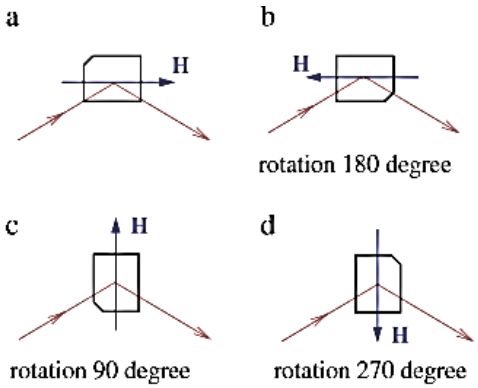

Fig. 17: Separation of the magnetization components using sample rotation. Magnetic field rotates together with the sample [47].

The polar and longitudinal Kerr rotation are separated using 180° rotation of the sample and magnetic field simultaneously. We can express the rotation as a sum of both effects

$$\theta_{\varphi} = A_1 \cdot M_L + A_2 \cdot M_P, \tag{9}$$

$$\theta_{\varphi+180^\circ} = -A_1 \cdot M_L + A_2 \cdot M_P, \tag{10}$$

where A_1, A_2 are the weight coefficients and generally $A_1 \neq A_2$. M_L stands for the longitudinal component of magnetization and M_P for the polar component of magnetization. After summation of (4) and (5) we obtain

$$A_2 \cdot M_P = \frac{1}{2}(\theta_{\varphi} + \theta_{\varphi+180^\circ}), \tag{11}$$

and after their subtraction

$$A_1 \cdot M_L = \frac{1}{2}(\theta_{\varphi} - \theta_{\varphi+180^\circ}). \tag{12}$$

Therefore summation and subtraction enables to separate polar and longitudinal components of MO effect. Similarly in the transversal components, we can separate in the same way the polar and transversal components (transversal components measured by longitudinal Kerr effect). The same procedure applies to Kerr ellipticity separation.

3.9.3. Separation of contributions from different depth (materials)

Based on additivity of MO effects it could be possible to separate MO contributions from different magnetic phases expressing measured signals. The dependence of the Kerr rotation θ_K and ellipticity ε_K on two magnetic phases is shown in the following. Based on linearity, we can write the relations between the vector of magnetizations **M** and the matrix of the weight coefficients **A** as follows [47]:

$$\mathbf{\Phi} = \begin{bmatrix} \theta \\ \epsilon \end{bmatrix} = \begin{bmatrix} A_{11} & A_{12} \\ A_{21} & A_{22} \end{bmatrix} \cdot \begin{bmatrix} M_1 \\ M_2 \end{bmatrix} = \mathbf{A} \cdot \mathbf{M}, \tag{13}$$

where M_1 and M_2 are the normalized magnetizations of two different phases[2]. Once the coefficients of **A** are determined, it is able to obtain the magnetization matrix describing both MO phases using the matrix inversion [48]:

$$\mathbf{M} = \mathbf{A^{-1}} \cdot \mathbf{\Phi}. \tag{14}$$

3.9.4 Measurement of MO spectra

Magneto-optical spectra measurements can be performed on Mueller matrix ellipsometer that was extended with an in-plane magnet circuit consisting of permanent magnet mounted on a rotary stage. The magnet is controlled by a servomotor via computer which ensured a reproducibility of the measurement. The permanent magnet in case of our measurements delivers magnetic field of 300 Oe sufficient for in-plane magnetic saturation of Bi:YIG samples. The magnetization is applied both, in longitudinal (LMOKE) and transversal (TMOKE) MO configuration. After each measurement of MO spectrum, the magnetization is reversed. Five measurements at every configuration with magnetization either up or down was done for each of two measured samples. Data were then averaged in order to reduce the noise. Subtraction of averaged data for opposite magnetization lead to the differential Mueller matrices [49]:

$$\boldsymbol{M}_x^{diff} = \boldsymbol{M}(+M_x^{sat.}) - \boldsymbol{M}(-M_x^{sat.}), x = T, L. \tag{15}$$

4. EXPERIMENTAL RESULTS

4.1. Prepared samples

The samples were prepared in two series with different compositions. Both series have got a composition of bismuth yttrium iron garnet. All samples are shown in Table 1 (first series) and Table 2 (second series) together with their deposition conditions.

Table 1: Prepared samples for the first series (Bi_2YIG) and their deposition conditions

First series - Bi_2YIG on GGG-(100)				
Thin film	Deposition temperature [°C]	**Heating voltage [V]**	**Oxygen pressure [mTorr]**	**Duration**
MBE190515	815	27	5	15 min
MBE200515	870	29	5	15 min
MBE210515	810	27	5	15 min
MBE220515	806	27	34	15 min
MBE260515	815	27	70	17 min
MBE270515	809	27	70	1 h 25 min

Table 2: Prepared samples for the first series (BiY_2IG) and their deposition conditions

Second series - BiY_2IG on GGG-(100)				
Thin film	**Deposition temperature [°C]**	**Heating voltage [V]**	**Oxygen pressure [mTorr]**	**Duration**
MBE100615	835	29	70	15 min
MBE120615	860	29	34	20 min 15 s
MBE150615	850	29	50	20 min

MBE160615	898	30	5	20 min
MBE170615	893	30	34	20 min
MBE180615	860	29	34	20 min
MBE190615	850	29	34	1h 03 min

In the first series, there is a content of two bismuth and one yttrium, and in the second series there is a content of one bismuth and two yttrium. All thin films were deposited on gadolinium gallium garnet substrate cut in (100) plane. All samples have got cubic crystal structure.

4.2. Scanning electron microscopy (SEM)

For purpose of studying chemical composition of the targets used as a source for laser ablation, the SEM analysis was done. The images (Fig. 18) were made by Cristele Vilar and the analysis, which can be seen in the following graphs (Fig. 19), was done by myself.

The target was rotating during the deposition and moving in y axis (up and down). The target surface after several depositions (one series of thin films) can be divided into three parts. Next two figures (Fig. 18 and Fig. 19) show results for the target of the first series ($Bi_2YFe_5O_{12}$)**.** In the pictures (A) and (E) in Figure 5 the non-ablated area (edges of the target) can be seen. All other pictures correspond to the ablated areas. The picture (C) shows the center of the target, and (B) and (D) shows the edges of the ablated area (between the center of the target and its edges).

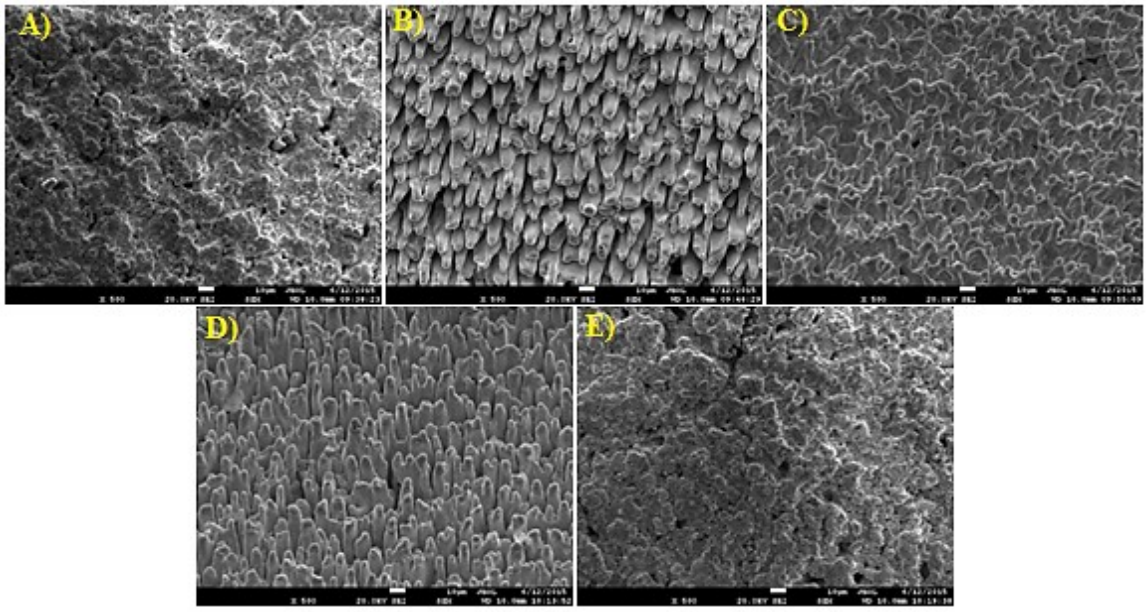

Fig. 18: SEM pictures of the first target - $Bi_2YFe_5O_{12}$: A), E) non-ablated areas; B), C), D) ablated areas.

Different areas of the target shown in Fig. 18 indicate that the trace of the laser beam hitting the target during the deposition is not homogeneous. Laser beam hit the center of the target more than the edges. Thus, the deposited elements are ablated much faster from the center of the target which confirms analysis done in Fig. 19. In Figure 19, we can see the content of elements in the target as a function of a position on the target. When we look on the graph showing the chemical composition, we can see we lost oxygen and bismuth in the ablated area. The analysis in the second panel of Fig. 19 shows how the Bi to Y ratio, Bi to Fe ratio and Y to Fe ratio changed with the position on the target. The curve corresponding to Bi/Y ratio is more deepened in the ablated area and the same trend can be seen in the curve corresponding to Bi/Fe ratio. Y/Fe ratio does not change significantly. Thus, we could conclude that bismuth was evaporating much faster than yttrium in the middle of the target.

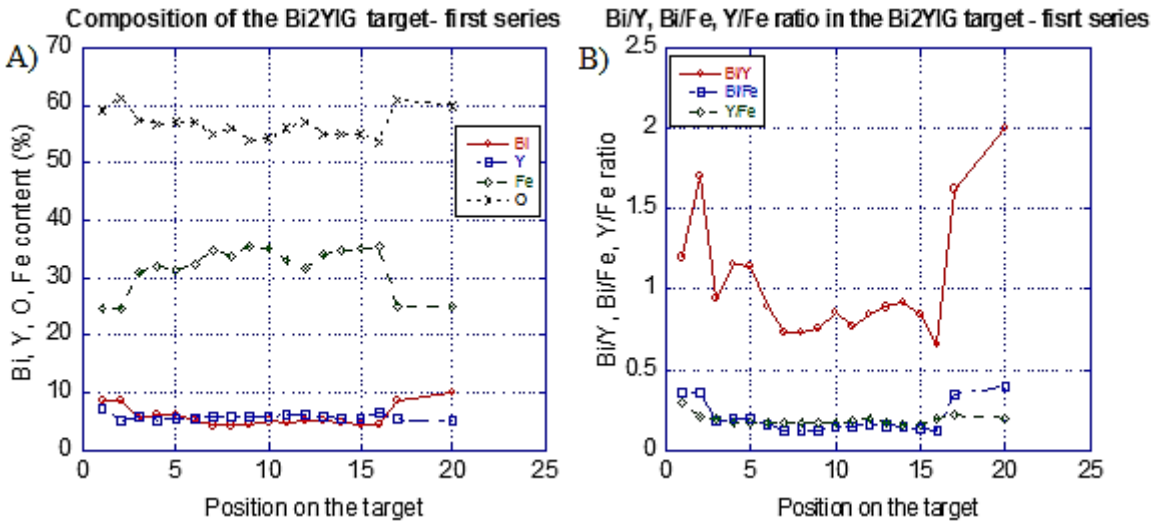

Fig. 19: Analysis of composition of the target from the first series. A) Bi, Y, O, Fe content as a function of position on the target, B) Bi/Y, BI/Fe, Y/Fe ratio as a function of position on the target.

For the second target, exactly the same analysis was done. When we look at the pictures in Figure 20 we can see that the morphology before and after ablation of the target was very similar to the morphology of the first target. Again, on the edges of the ablated area (B) and (D), there were some kind of needles and in the center of the target (C) the surface looked melted. That means that there was higher temperature in the center than closer to the edges.

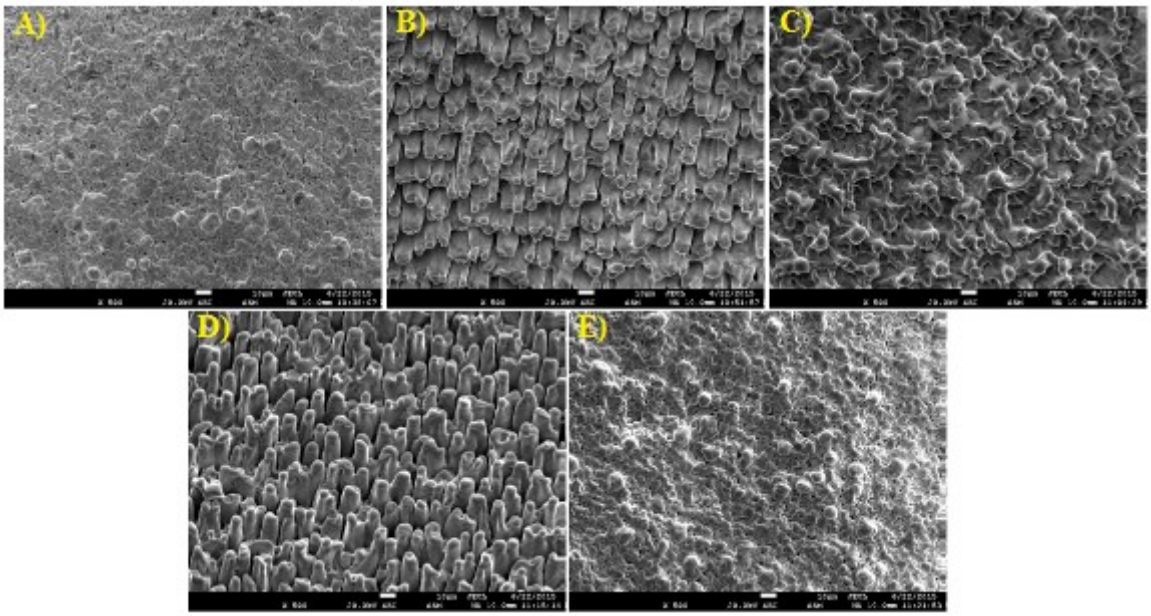

Fig. 20: SEM pictures of the second target - $BiY_2Fe_5O_{12}$. A), E) non-ablated areas; B), C), D) ablated areas.

The analysis of the composition as a function of position on the target for the second target (Fig. 21 – A) showed the same trends, and the analysis for the ratios (Fig. 21 – B) as well. Anyway, in the second graph (Fig. 21 – B), we can see even more deepened curve for Bi/Y ratio and Bi/Fe ratio, which confirms that we had even less bismuth in this target after ablation.

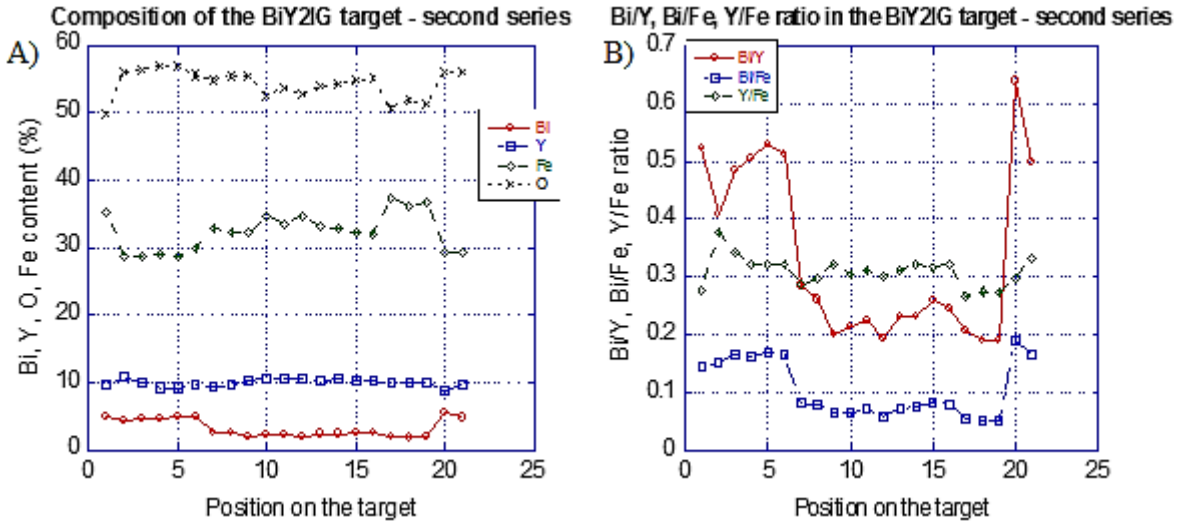

Fig. 21: Analysis of composition of the target from the second series. A) Bi, Y, O, Fe content as a function of position on the target, B) Bi/Y, Bi/Fe, Y/Fe ratio as a function of position on the target.

The inhomogeneous ablation of the targets result in their limited lifetime. Chemical composition analysis confirmed the SEM analysis and showed that Bi evaporates faster than yttrium or iron from the target during the deposition so the targets need to be changed more frequently.

4.3. Emission spectroscopy

Chemical composition of plasma ions during deposition was detected using emission spectroscopy. Figure 22 shows a spectrum of plasma captured during a deposition. It shows an intensity plotted as a function of wavelength. The positions of the peaks which correspond to pure Bi, Y and Fe were found.

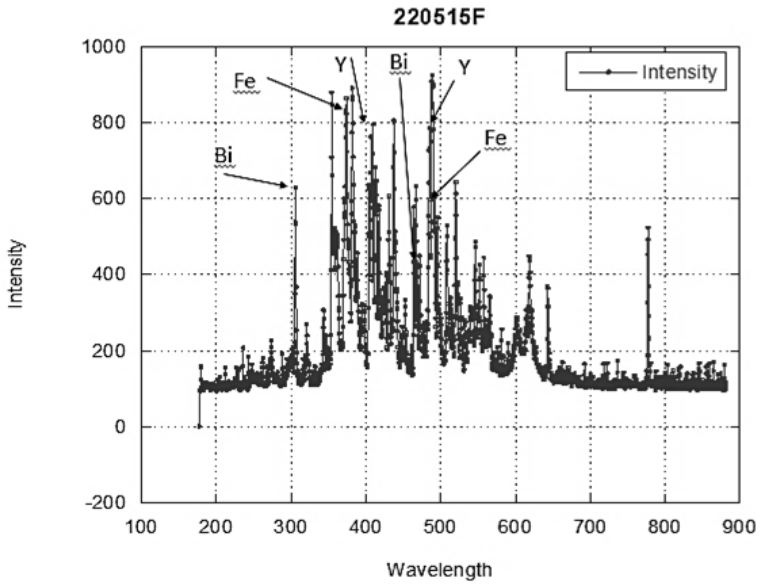

Fig. 22: Methodology of emission spectroscopy analysis.

The intensities of the peaks corresponding to the wavelengths of the peaks marked it Fig. 22 are shown in Table 3.

Table 3: Table of intensities of the peaks marked in Figure 22

Element	Wavelength [nm]	Arb. units	Wavelength [nm]	Arb. units
Bi	306	629	472	449
Y	410	795	485	785
Fe	373	865	495	548

The results of the analysis were following. The question was, how has the Bi content in plasma changed with the ablation time? In the first series of samples, several samples as a function of temperature and then several samples as a function of pressure were prepared. In Figure 23 – A), we can see the analysis of Bi/Y ratio as a function of ablation time. The Bi/Y ratio got smaller with increasing pressure. In the second graph (B), we can see the same analysis but for Bi/Fe and Y/Fe ratio. The ratio of Y/Fe was varying with pressure, too.

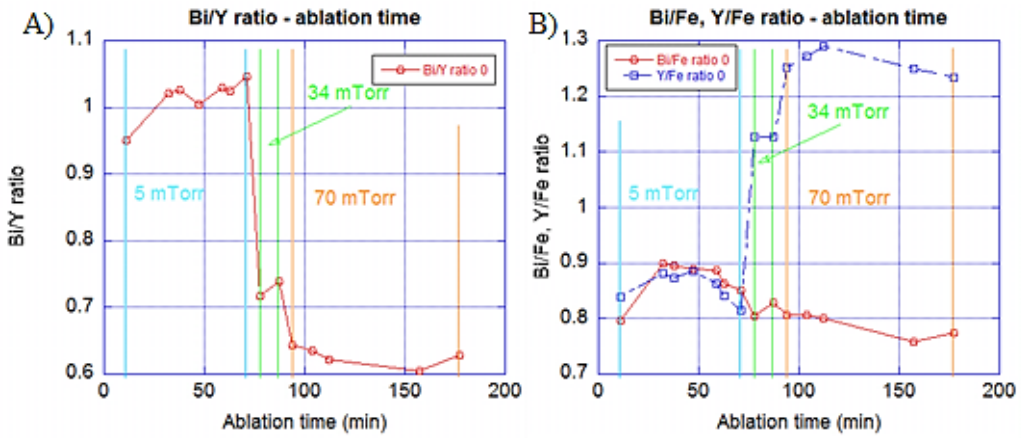

Fig. 23: Emission spectra analysis for the first target - $Bi_2YFe_5O_{12}$. A) Bi/Y ratio as a function of ablation time, B) Bi/Fe and Y/Fe ratio as a function of ablation time.

For the second target and second series of the samples, we can see again that the Bi/Y ratio and Y/Fe ratio changed with varying pressure (Fig. 24 – A), while Bi/Fe ratio remained almost constant (Fig. 24 – B).

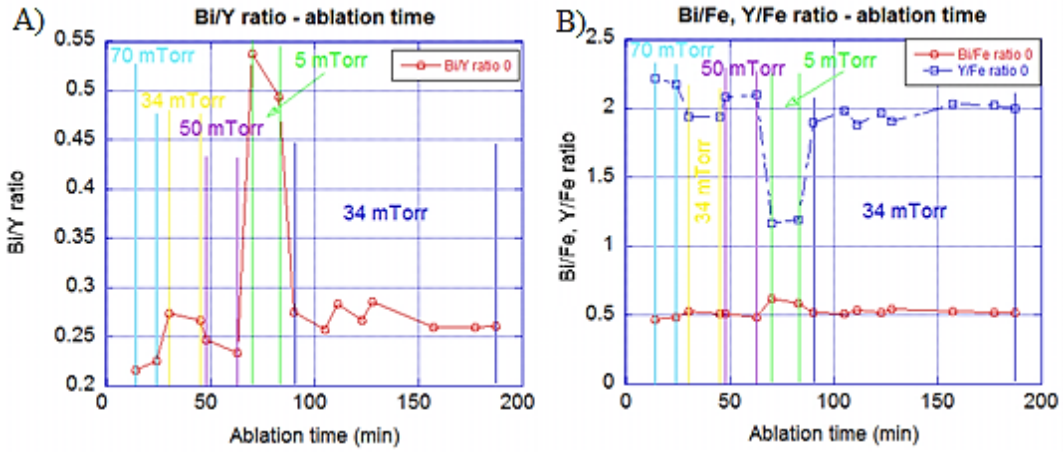

Fig. 24: Emission spectra analysis for the second target - $BiY_2Fe_5O_{12}$. A) Bi/Y ratio as a function of ablation time, B) Bi/Fe and Y/Fe ratio as a function of ablation time.

The answer to the question is that the bismuth content in plasma changed with pressure, not with the ablation time and if the oxygen pressure remained constant, Bi/Y and Y/Fe ratio was constant, too. Consequently, it seems that yttrium content in plasma is more dependent on pressure than bismuth content, as it was shown by comparing the analyzed ratios together.

4.4. Atomic force microscopy (AFM)

Next analysis was AFM analysis. The example of morphology of one sample from each series is shown (Fig. 25 and Fig. 26). Roughness was measured in the area of 10 x 10 μm and then it was also measured in the boxes, without the big grains. We can see that there were some big grains on the surface of the samples which increased the overall roughness, while the roughness measured in the boxes was significantly smaller.

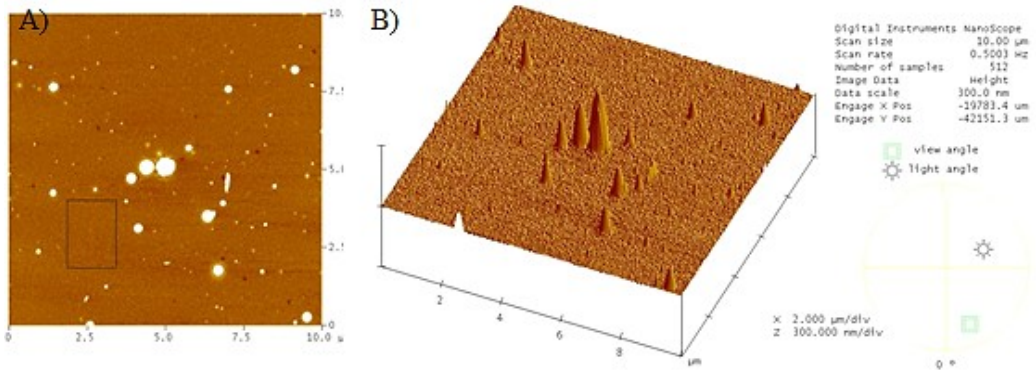

Fig. 25: An example of morphology of the best sample from the first series. A) MBE200515, 10 x 10 μm: Rms = 12.694 nm, **Rms box = 1.437 nm nm** (area without strong peaks, denoted by black rectangle), B) 3D image of rough surface.

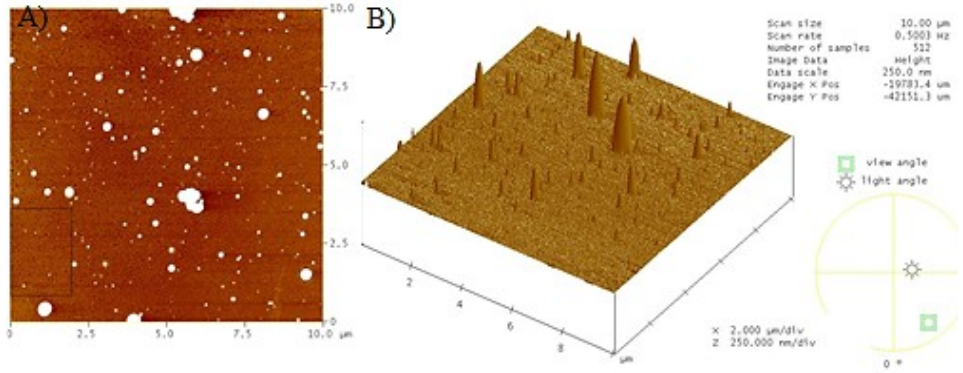

Fig. 26: An example of morphology of the best sample from the second series. A) MBE180615, 10 x 10 μm: Rms = 20.486 nm, **Rms box = 1.273 nm** (area without strong peaks, denoted by black rectangle), B) 3D image of rough surface.

Figure 27 show the roughness analysis where Rms was plotted as a function of substrate temperature and pressure during the deposition for the first series, and as a function of sample name for the second series.

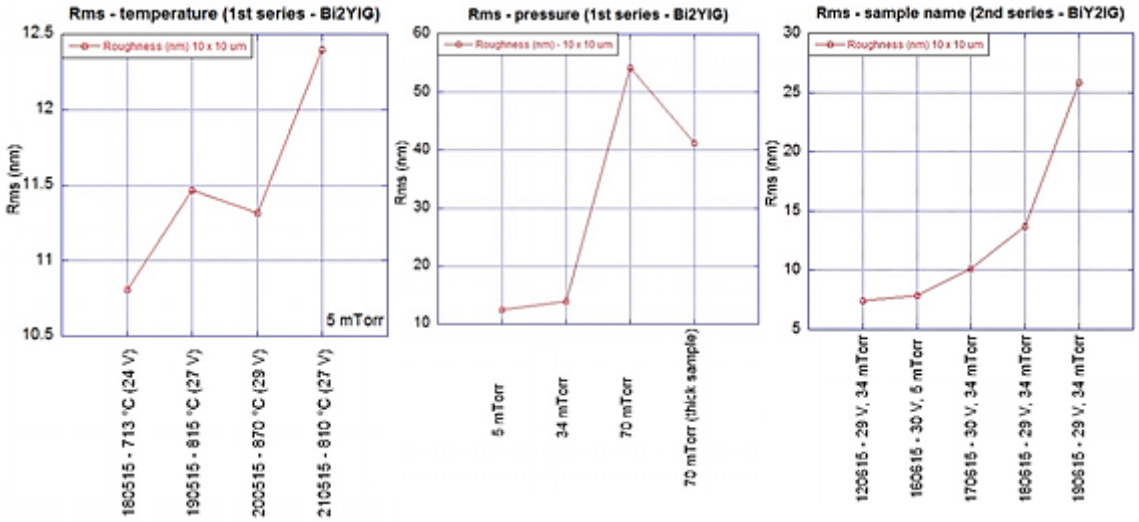

Fig. 27: Roughness analysis – RMS as a function of A) temperature, B) pressure, C) samples sequentially ablated from the same target.

We can see that the roughness was increasing in every case, so it might be a consequence of increasing amount of grains (needles from the target) on the surface with longer ablation time of the target. So the more ablated the target was, the rougher was the overall surface. Hence, the dependence only on the temperature or the pressure could be questionable. Anyway we could say that the roughness is more dependent on the pressure, than on the temperature. The reason could be that the lower pressure enables more needles ablated from the target to land on the substrate.

4.5. X-ray diffraction (XRD)

Crystal structure of the samples was studied using X-ray diffraction (XRD) and the diffraction pattern of the best sample from second series for (400) peak is shown in Figure 28. The peak at 28.5° corresponded to the film and the peak at 28.8° corresponded to the substrate. In the blue circle we could see some extra oscillation which might be the Laue oscillation.

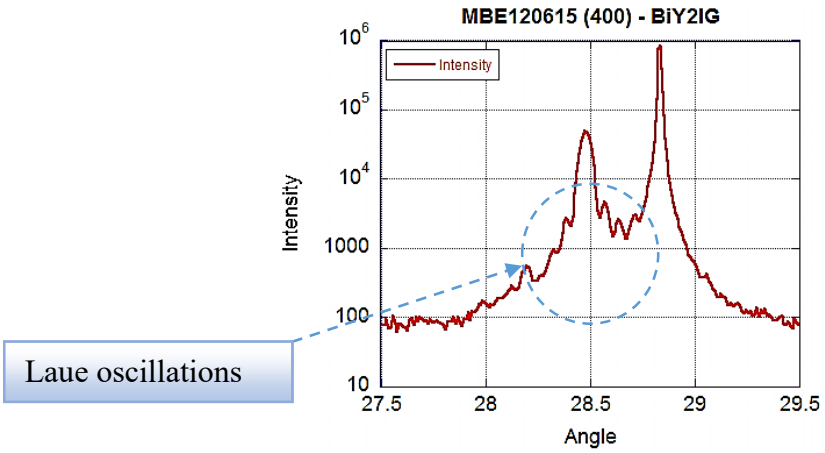

Fig. 28: Diffraction pattern for the best sample from the second series with Laue oscillations.

The next step was to make a simulation of Laue oscillations (Fig. 29) and confirm that we have got samples with good structure.

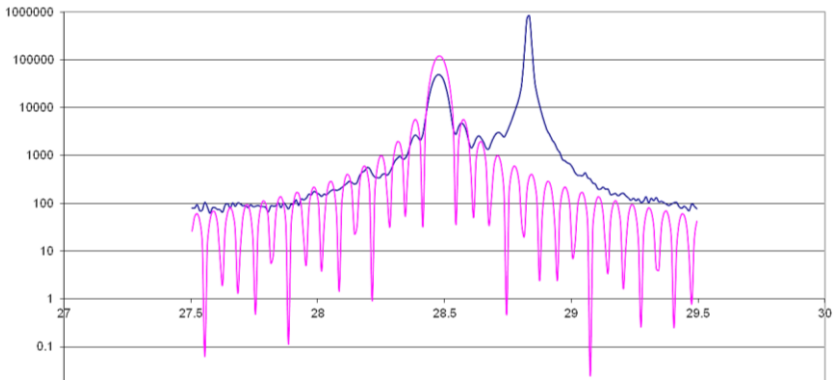

Fig. 29: Laue oscillations observed in the film MBE120615 around (400) peak.

The simulation in Figure 29 fitted relatively well to the diffraction pattern near the central peak which means that our film has well crystalized and was homogeneous in thickness. The grains were oriented in the same direction and the thickness measured here corresponded to the thickness measured with profilometry. The simulation simulates perfectly smooth surface and thus the real oscillations measured by XRD probably attenuate due to the roughness on the surface of the sample.

Figure 30 shows the lattice constants obtained from XRD analysis. There were plotted lattice parameters as a function of pressure and temperature for the first series (A, B) and as a function of sample name for the second series (C).

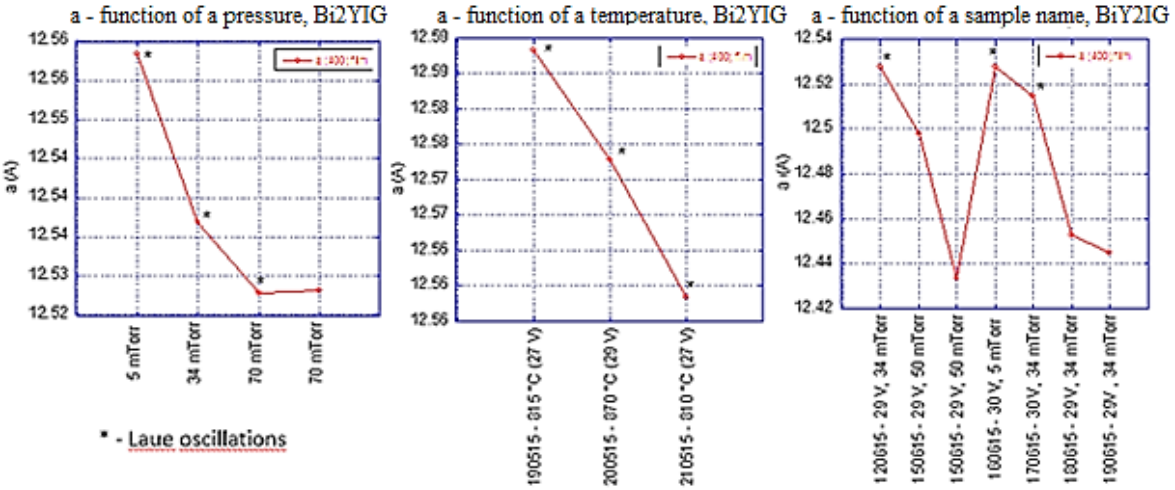

Fig. 30: Out of plane lattice parameters as a function of A) pressure, B) temperature, C) sample name.

In Figure 30, we can easily see that the lattice parameter decreased with increasing pressure (A) which was also confirmed by different authors. Lattice parameter as a function of temperature or the sample name did not show significant dependence. However, at the same deposition conditions, the lattice parameter decreases as a function of the sample name (C), which could be connected to the target wear, and thus slightly different stoichiometry in the resulting films. Samples marked with the stars were those at whose diffraction patterns the Laue oscillations appeared so the best crystalized samples.

4.6. RHEED, in-situ ellipsometry, profilometry

In-situ techniques used before and after every deposition were ellipsometry and RHEED.

RHEED technique was used first to determine in-plane lattice parameter of pure substrate, and after the deposition to determine the crystallization of new thin film and its in-plane lattice parameter. This procedure was done for each prepared sample and a graphical lattice reconstruction was performed after recording the RHEED images (Fig. 31).

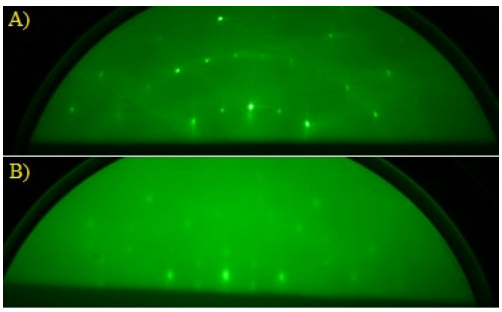

Fig. 31: An Example of RHEED picture of A) GGG substrate and B) BYIG thin film.

The lattice parameter was determined bigger in compare to the value obtained from single crystal GGG substrate That was probably caused by not very precise set up – it was usually needed to tilt the sample to obtain the RHEED image but as for the real scientific attitude, the tilt should not be touched. Thus, this technique was used, except of the information mentioned above, only for rough information about crystal quality of growth

In situ ellipsometry was only used to measure the thickness in the middle of the sample and the results were used to have the first idea of the thickness of the sample and then they were compared to the results obtained by the profilometry technique.

Ex-situ **profilometry** was used to determine thickness on the edges for all samples and to get the first idea about the roughness. The results were put in a data table (Table 4).

Table 4: Profilometry results showing thickness of all prepared samples

Sample	Thickness [nm]	Sample	Thickness [nm]
MBE180515	133 ± 3	MBE100615	390* ± 14
MBE190515	152 ± 3	MBE120615	137 ± 5
MBE200515	128 ± 5	MBE150615	107 ± 14
MBE210515	144 ± 4	MBE160615	177 ± 2
MBE220515	125 ± 5	MBE170615	151 ± 6
MBE260515	150 ± 8	MBE180615	135 ± 6
MBE270515	570 ± 20	MBE190615	436 ± 12

*after annealing because of bad crystallization

4.7. Magneto-optical results – Faraday effect

At first, Faraday rotation and ellipticity for samples from the first series were measured. In Figure 32, we can see how the Faraday rotation and ellipticity of the thin films from the first series depend on the deposition conditions.

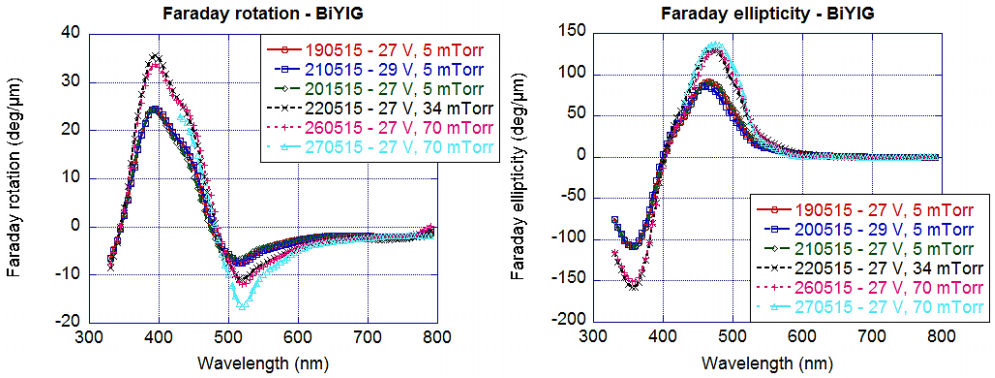

Fig. 32: Magneto-optical measurements for the first series of the samples. A) Faraday rotation as a function of wavelength, B) Faraday ellipticity as a function of wavelength.

With increasing temperature (voltage), the quality of film increased a little bit. Increasing the pressure, the amplitude increased significantly for both, ellipticity and rotation. Higher pressure also led to a better stoichiometry which was confirmed with plasma analysis (emission spectroscopy).

For the second series, the same measurements were done and we can see even better the Faraday rotation and ellipticity dependence on pressure (Fig. 33). For example, the amplitude was quite low for 5 mTorr but it got higher with higher pressure. The little shift, which can be seen between the curves, was probably caused either by different stoichiometry of the thin films (more Bi with increasing pressure), or by the effect of two sublattices in the crystal structure.

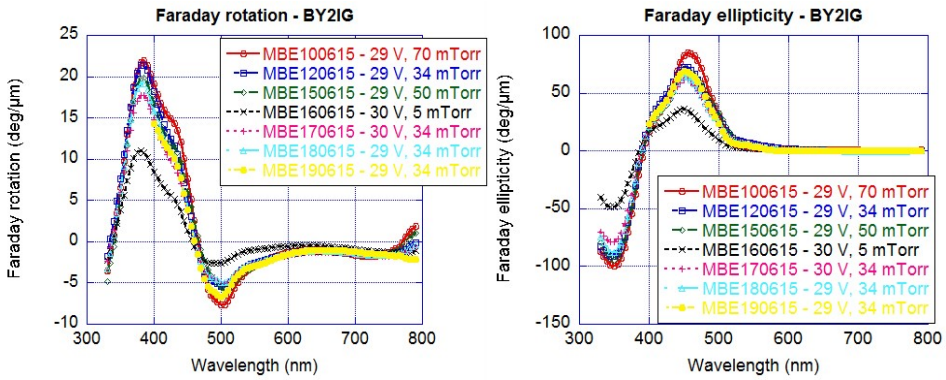

Fig. 33: Magneto-optical measurements for the second series of the samples. A) Faraday rotation as a function of wavelength, B) Faraday ellipticity as a function of wavelength.

Next, a comparison of magneto optical response from the samples with a composition varying from pure YIG to pure BIG is shown (Fig. 34).

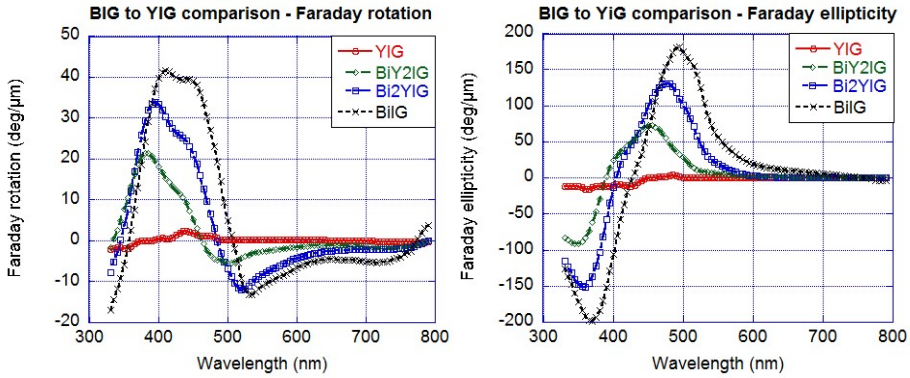

Fig. 34: A comparison of A) Faraday rotation, B) Faraday ellipticity of the samples with different compositions.

In Figure 34, we can see how the amplitudes with compositions from pure YIG to pure BIG changed. Resulting from the graphs, the more bismuth we had, the higher was the amplitude, and the amplitude increased regularly with bismuth addition. This is related to the fact, that BIG exhibit an order of magnitude stronger Faraday rotation and pure YIG.

If we compared the gaps between single amplitudes, we could see a bigger gap between pure YIG and BiY_2IG than between the others, where the change was approximately the same width. So we could conclude that the nominal content of Bi in our samples was higher

than we expected which was also confirmed by the Curie temperature measurements shown next.

The last measurement in this section was Curie temperature measurement which was done only for the best samples, one from the first series and one from the second series (Fig. 35). For the best sample from the first series the Curie temperature was determined at 637 K (A) and for the best sample from the second series the Curie temperature was 602 K (B). The Curie temperature was in agreement with lower Bi content used in the second series.

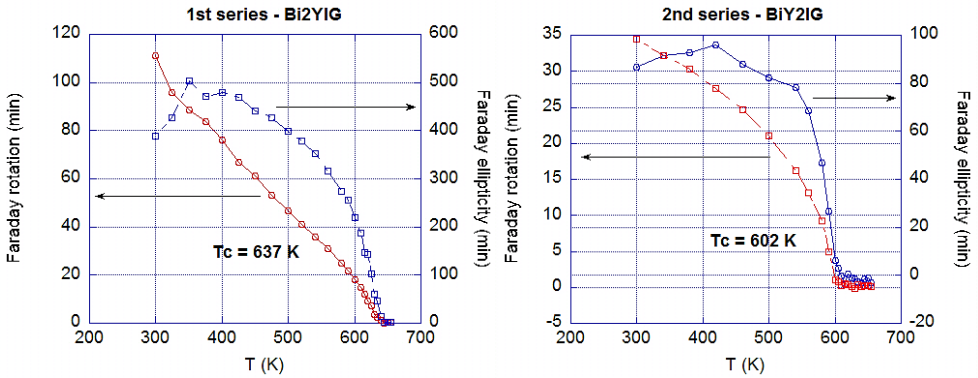

Fig. 35: Measurements of Curie temperature for the best sample from A) the first series, B) the second series.

Determined values of Curie temperature were compared with literature, where there was found that Bi content was higher in each sample than expected from Curie temperature dependence. For the first series, the sample has got 2.35 Bi content and for the second series the sample would have got 1.32 Bi content (Fig. 36).

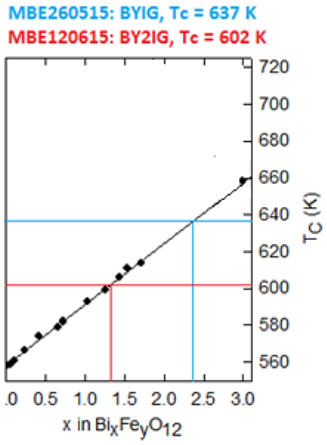

Fig. 36: Comparison of Curie temperature of the best samples with literature [1].

4.8. Spectroscopic ellipsometry

Both thick samples (MBE270515 and MBE190615) were measured at the range from 25 to 60 degrees with 5 degrees step with a collimated light beam. Both samples are rough and basic models are no longer applicable for correct description of the physical behavior of the samples. Thus, more complex models were used and described below. One of the layer models is a B-spline layer developed in Complete Ease. It benefits from reduced number of fit parameters and flexibility in optical constants (we are able to fit any material). It helps significantly with parametrizing the dielectric functions. The main ability of the model is to maintain Kramers-Kronig consistency. For more information about B-spline see [50].

MBE190615 - model

Physical model for the sample MBE190615 consists of two layers according to Fig. 37. The optical functions of the main layer are described with B-spline function. The upper part of BiY_2IG layer is described using the effective medium of BYIG (parameterized by B-spline) and void. The volume fraction of the void of 3.7% was obtained from the data fit. The EMA layer model was needed to describe the surface of the layer probably due to high surface roughness or surface depth inhomogeneity. Roughness was included in the model and the optical functions of the substrate were taken from a tabulated values

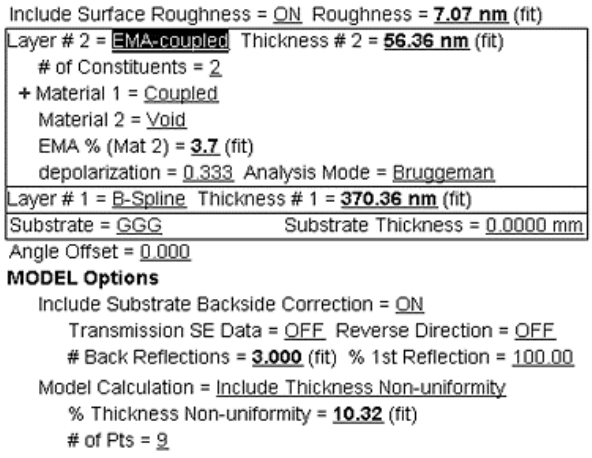

Fig. 37: Model parameters for the sample MBE190615.

Table 5: Model and layer properties for the sample MBE190615

MSE	Thickness non-uniformity	Back reflections	IR Amp.
5.262	10.3 ± 0.1 %	3 ± 4.6 %	0.00042368
Roughness	**Thickness # 1**	**EMA # 2 (Mat 2) %**	**Thickness # 2**
7.1 ± 0.1 nm	370.4 ± 0.5 nm	3.7 ± 0.1	56.4 ± 0.5 nm

In the model, there were backside reflections included (because of collimated light beam reflects both from upper side and back side of the substrate). In order to obtain a reasonable fit a thickness non-uniformity was included. This means that the thin film might not be deposited in every spot with the same thickness, or the substrate was cut slightly askew and so it affects the measurement. The sample was placed parallel with the holder and perpendicular to the plane of incidence of light. The film was not simultaneously fitted with transmission.

MBE190615 – Results

Figure 38 and Figure 39 show ellipsometric angles psi and delta fitted for the angles of incidence from 25 to 60 degrees. Figure 40 shows depolarization fitted for angle of incidence from 25 to 60 degrees.

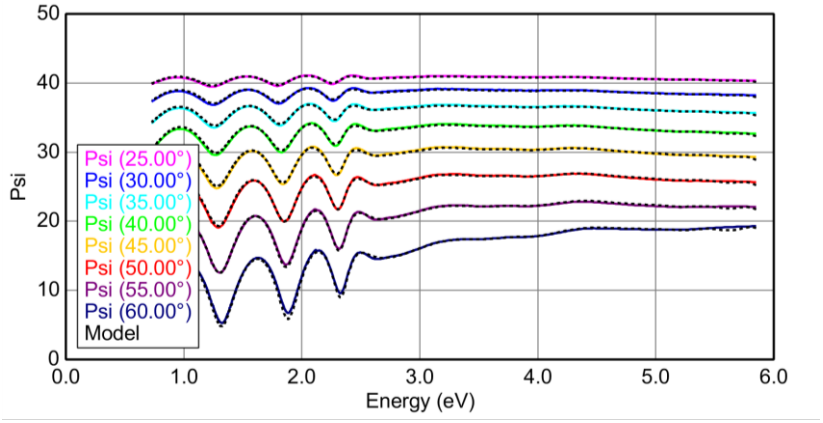

Fig. 38: Ellipsometric angle psi fitted for angle of incidence from 25 to 55 degrees.

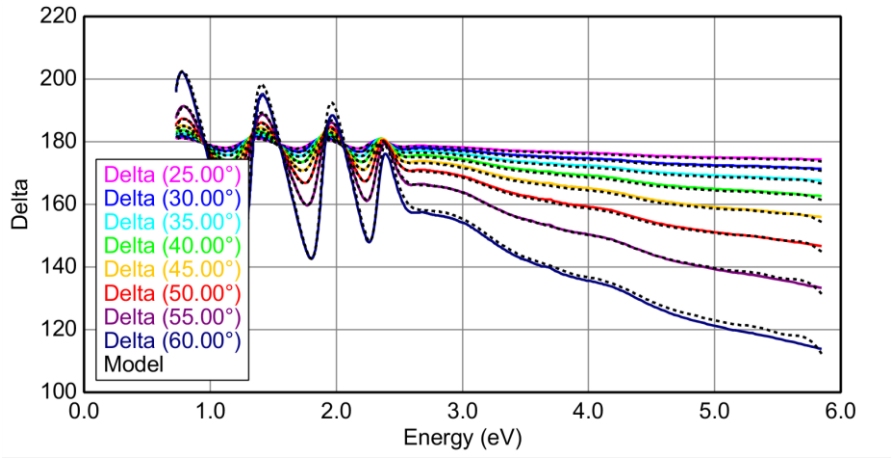

Fig. 39: Ellipsometric angle delta fitted for angle of incidence from 25 to 55 degrees.

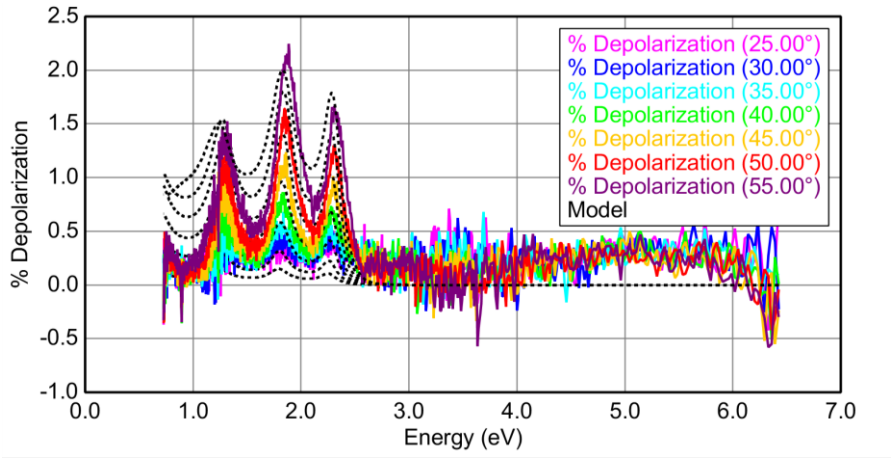

Fig. 40: Depolarization fitted for angle of incidence from 25 to 55 degrees.

Depolarization origin from incoherent summation of back-side reflection from the substrate. From the above graphs we can see that the material absorbs from the wavelength around 2.7 eV (460 nm). That is confirmed in the following graph showing the optical constants of the Bi_2YIG layer (Fig. 41.)

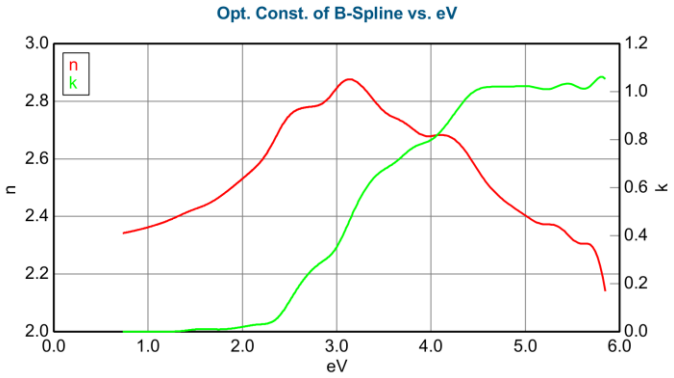

Fig. 41: Optical constants n and k of B-spline layer (Layer # 1).

Thickness of the sample was measured by profilometry and roughness by AFM. The results of these methods are compared with ellipsometric results. All data measured by ellipsometry were fitted together to a model. The best fitted parameters for MBE190615 sample show that model corresponds to measured data nicely and the material's optical constants are reasonable (Fig. 41).Roughness on the top of the surface is 7.1 ± 0.1 nm and it most likely corresponds to the biggest grains originating from the deposition process. EMA-Coupled layer seems to be more homogeneous and describes either the roughness on the surface without the biggest grains, or, most likely, a special layer 56.4 ± 0.5 nm thick containing 3.7 ± 0.5 % of air. This model seems to describe rather structural effect when there is a layer containing little cracks or grains with little vacancies between them. The roughness profile seems to be in correspondence with AFM images of the sample surface shown in Fig. 42.

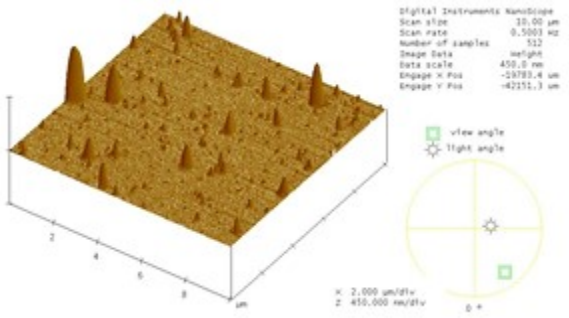

Fig. 42: AFM picture of the sample MBE190615 showing the roughness of the surface.

Thickness of the basal layer is 370.4 ± 0.5 nm. It was measured that the overall thickness varies throughout the sampe surface by 10.3 ± 0.1 %, so we may say that the sample is not homogeneous in thickness. Thickness measured by profilometry was determined to be 436 ± 12 nm, so it nearly corresponds to the total thickness determined by ellipsometry which is 433.8 nm.

MBE270515 - model

Physical model for the sample MBE270515 needed to be more complex. The model consists of three layers according to Fig. 43. The optical functions of the main layer are described with B-spline function. The upper part of Bi_2YIG layer is described using the effective medium of BIYG (parameterized by B-spline) and void. The EMA layer model was needed to describe the surface of the layer again due to high surface roughness or surface depth inhomogeneity, and thus its physical properties. However, two EMA model layers describing two types of upper layers, including the roughness were needed in this case. The volume fractions of the void of 20.1 % and 80.9 % were obtained from the data fit for the layer #2, and layer #3. Roughness was not included in a model and the optical functions of the substrate were taken from a tabulated values. Model was firstly applied to part from approx. 1.1 to 1.6 eV and then fitted by Expansion Wavelength Fit (wavelength after wavelength with a step 0.3 eV). Data were measured within the range from 25 to 60 degrees with collimated beam.

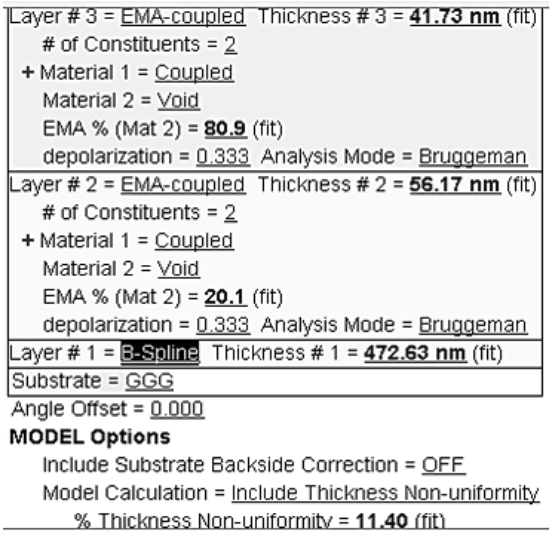

Fig. 43: Model parameters for the sample MBE270515.

Table 6: Model and layer properties for the sample MBE270515

MSE	Thickness non-uniformity	IR Amp.	Thickness # 1
2.887	11.40 ± 0.1 %	0.058	472.6 ± 1 nm
EMA # 2 (Mat 2)	**Thickness # 2**	**EMA # 3 (Mat 2)**	**Thickness # 3**
20.1 ± 0.3 %	56.2 ± 0.4 nm	80.9 ± 0.6 %	41.7 ± 0.4 nm

In the model, there are backside reflections off (the model better describes the measured data) and there was calculated a thickness uniformity, too.

MBE270515 Results

Figure 44 and Figure 45 show ellipsometric angles psi and delta fitted for the angles of incidence from 25 to 60 degrees. Figure 45 shows depolarization fitted for angle of incidence from 25 to 60 degrees.

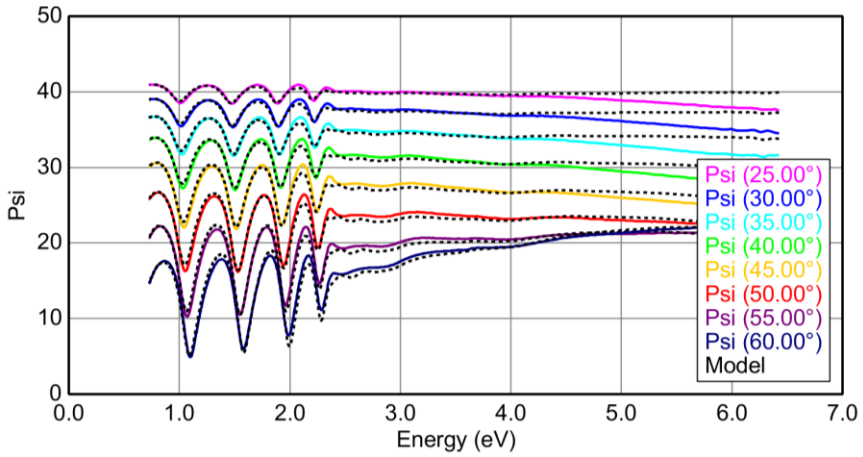

Fig. 44: Ellipsometric angle psi fitted for angle of incidence from 25 to 60 degrees.

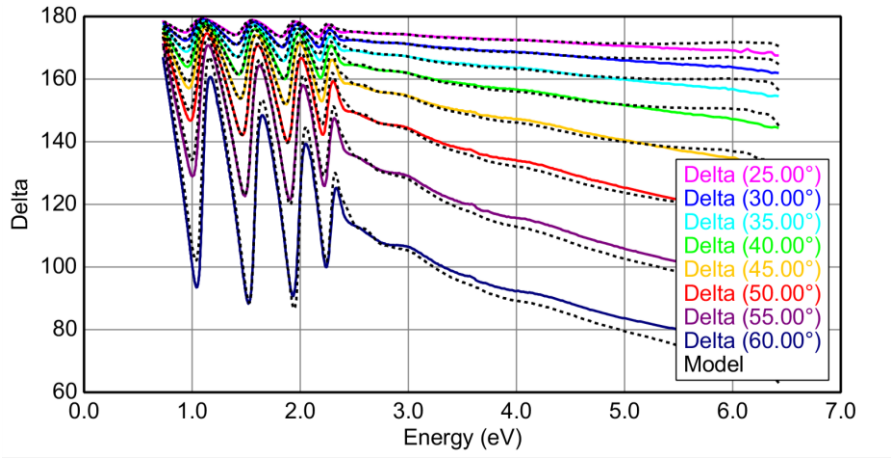

Fig. 45: Ellipsometric angle delta fitted for angle of incidence from 25 to 60 degrees.

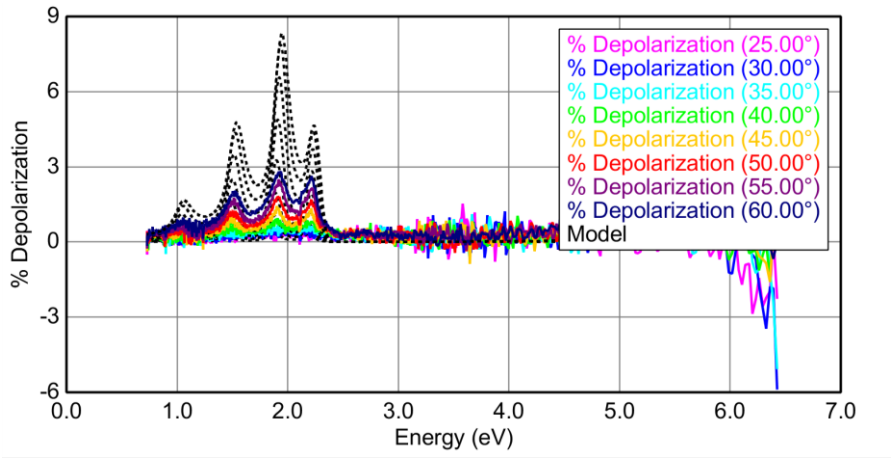

Fig. 46: Depolarization fitted for angle of incidence from 25 to 60 degrees.

Depolarization origin from incoherent summation of back-side reflection from the substrate. From the above graphs we can see that the material absorbs from the wavelength around 2.4 eV (516 nm). That is confirmed in the following graph showing the optical constants of the Bi_2YIG layer (Fig. 47.)

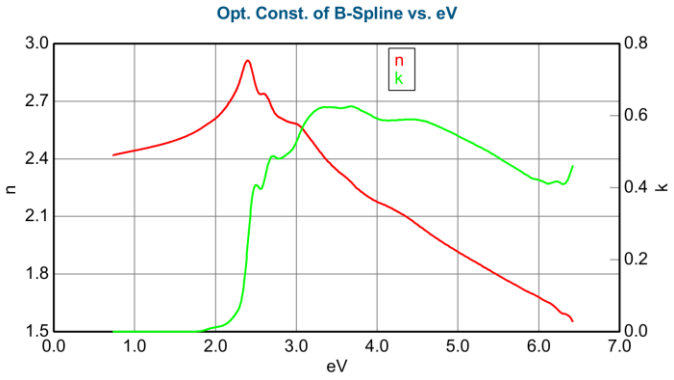

Fig. 47: Optical constants n and k of B-spline layer (Layer nr. 1).

The model for the sample MBE270515 corresponds to measured data relatively well according to MSE (Mean Squared Error), and the material's optical constants are reasonable. EMA describes two layers. The middle layer (# 2) is 56.2 ± 0.4 nm thick and contains 20.1 ± 0.3 % of air. That shows denser material but still containing some air, which implies either roughness without many bigger grains originating from the deposition process, or grains of material deposited close to each other creating a layers with little cracks or vacancies between them. The second layer described by EMA (# 3) is 41.73 ± 0.4 nm thick and contains 80.9 ± 0.6 % of air. That corresponds to the layer with the biggest grains and could be considered as the surface roughness. These results might be in conformity with the results of AFM measurement (Fig. 48).

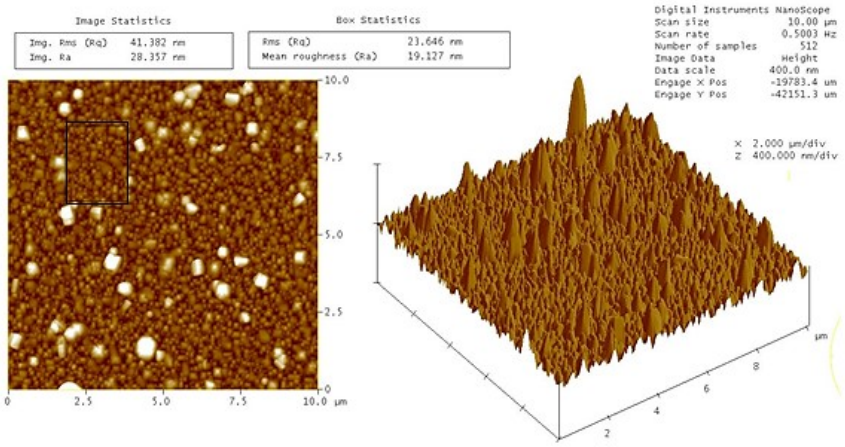

Fig. 48: AFM picture of the sample MBE270515 showing the roughness of the surface.

Thickness of the basal layer is 472.6 ± 1 nm. There was measured that the overall thickness varies throughout the sampe surface by 11.4 ± 0.1 %, so we may say that the sample is not homogeneous in thickness, too. Thickness measured by profilometry was determined to be 570 ± 20 nm, so it nearly corresponds to the total thickness determined by ellipsometry which is 570.5 nm.

Comparing the samples, the sample MBE270515 was more difficult to describe, than the sample MBE190615. Anyway, both samples were shown as rough when trying to aply simpler models to describe its interesting physical properties. Such models were no longer applicable for roughnesses above 50 nm. Thus, in both cases, the model was put together from tabulated GGG substrate optical constants, B-spline layer, and EMA which represents a complex description based on the mixture of basal layer and air.

The chosen models represented the best option how to describe the behaviour of given samples. The second sample (MBE270515) was more difficult to describe by ellipsometry, as well as by magneto-optical measurements, than the first sample (MBE190615). This statement is to be confirmed with magneto-optical measurements of MOKE in the next section.

Results from ellipsometry correspond to the results from AFM and profillometry. Optical constants of Bi:YIG layers obtained in both data fits correspond to those found in literature [49].

4.9. MOKE, separation of magnetic components

The same samples as for the ellipsometry analysis above were measured for magneto-optical Kerr effect (MOKE) on the MO setup described in chapter 3.9. Results are explained on one example: longitudinal loops measured at 000° and 180°, and transversal loops measured at 090° and 270°.

MBE270515 – results – s-polarization

Figure 49 shows the original measured MO hysteresis loops of Kerr rotation and Kerr ellipticity measured at s-polarization for primary reflected laser beam. The hysteresis loops were measured at longitudinal configuration for 0° and 180 °.

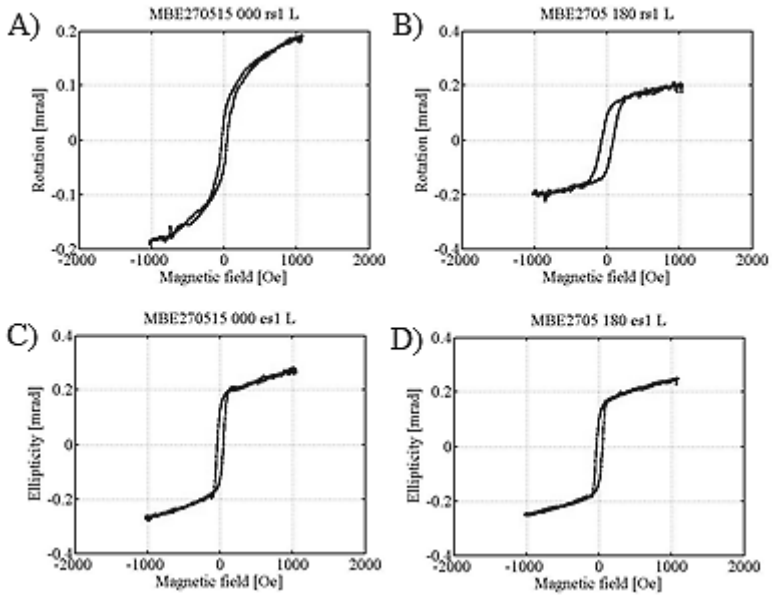

Fig. 49: Hysteresis loops - longitudinal configuration, s-polarization, A) Kerr rotation at 0°, B) Kerr rotation at 180°, C) Kerr ellipticity at 0°, D) Kerr ellipticity at 180°.

Figure 50 shows the original measured MO hysteresis loops at s-polarization for primary reflected laser beam measured at transversal configuration for 90° and 270°.

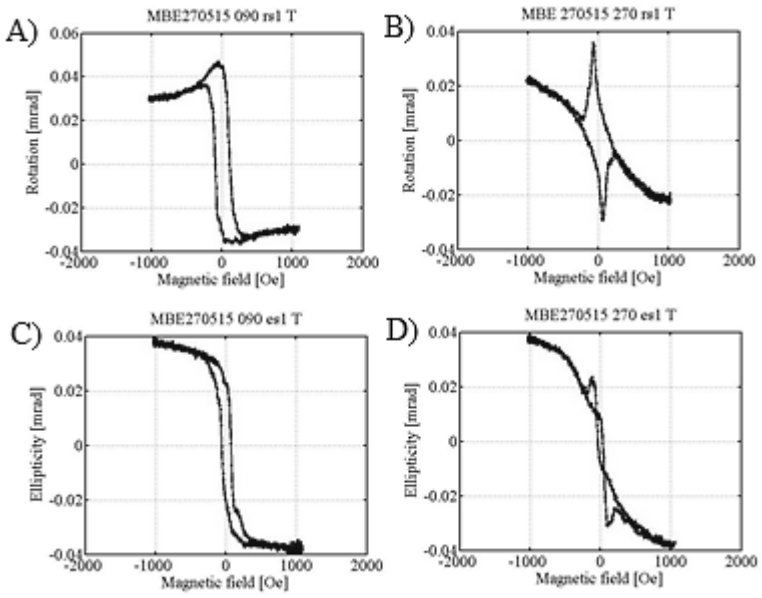

Fig. 50: Hysteresis loops - transversal configuration, s-polarization, A) Kerr rotation at 90°, B) Kerr rotation at 270°, C) Kerr ellipticity at 90°, D) Kerr ellipticity at 270°.

The different shapes of the loops show evidence of polar contribution to the hysteresis loops. Figure 51 show separated magnetic components (using (9), (10)) for s-polarization and primary reflected laser beam.

polar component **longitudinal component** **transversal component**

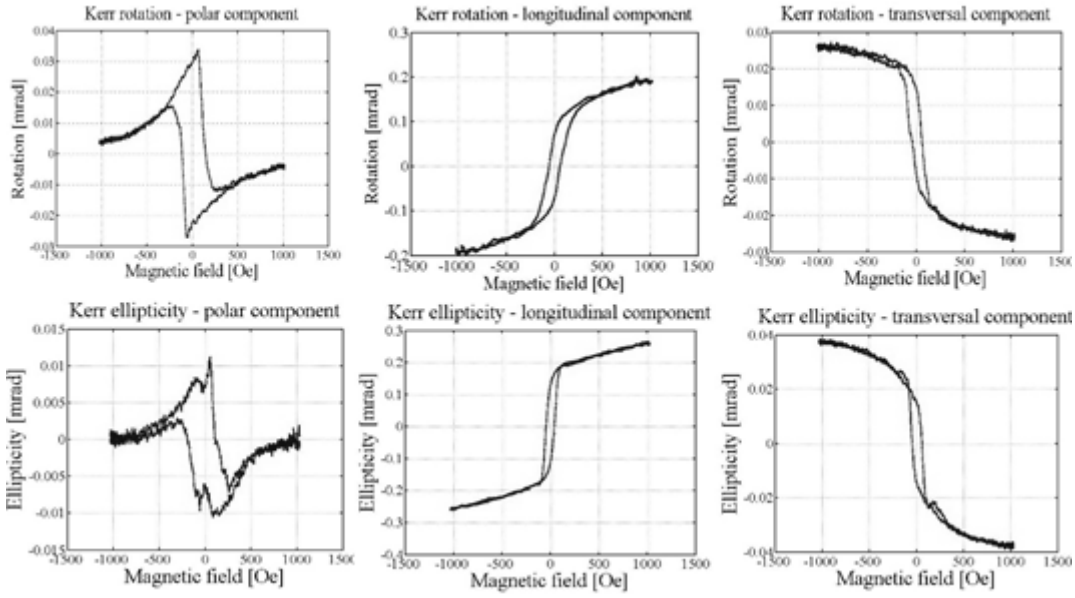

Fig. 51: separated magnetic components for s-polarization, primary reflected laser beam. Polar longitudinal and transversal component of Kerr rotation (upper row), and Kerr ellipticity (bottom row).

From the above separated magnetic components we can deduce that there is not negligible polar contribution with polar remanence for both, Kerr rotation and Kerr ellipticity. It is worth mentioning that the polar loops obtained in longitudinal and transversal configuration were almost the same which was an independent check of separation validity. Comparing the transversal component with the longitudinal one, the transversal is negligible, though, a small remanent transversal component is noticeable. It probably appear by non-perfect adjustment of the incident plane, magnet, and incident polarization. Thus, for the next measurements, the transversal component will not be presented. According to the longitudinal components, the magnetization in the sample lies mainly in-plane. However, a small remanent polar component is present and decreases for higher external magnetic field. That could indicate that there exists a magnetic domain structure in the sample. In some of those small magnetic domains, when changing the direction of the magnetization, the

magnetization rotates through the polar configuration and thus the minimal polar effect occurs.

The difference between the first and the second reflection is demonstrated on longitudinal effects shown below (Fig 52 and Fig. 53), where we study the dependence on the sample rotation (in-plane sample anisotropy). Longitudinal components were separated from the hysteresis loops measured at 0°, 90°, 180, and 270°.

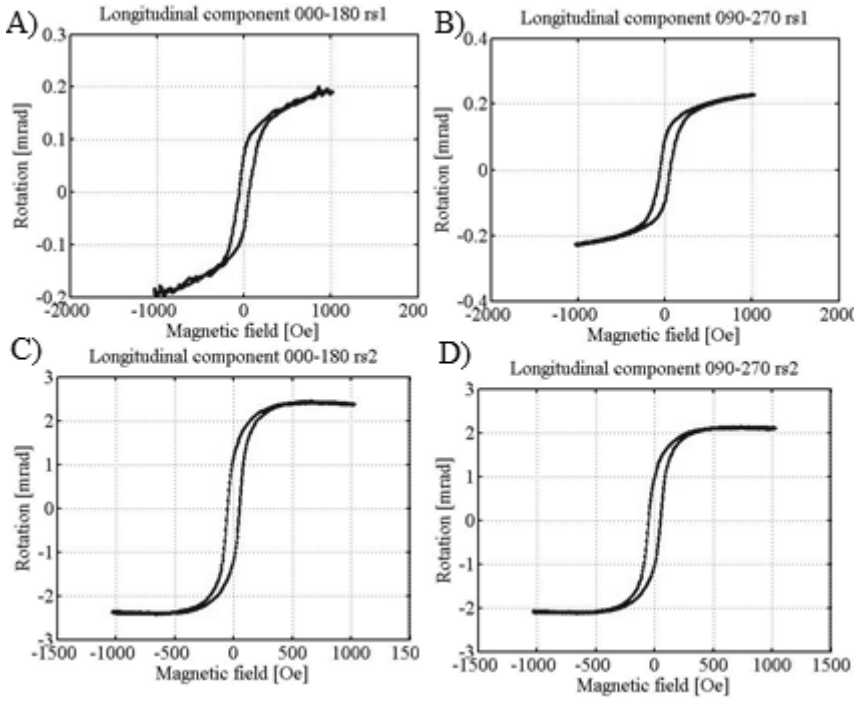

Fig. 52: Comparison of longitudinal effects for the Kerr rotation for primary (A, B) and secondary (C, D) reflected beam at s-polarization.

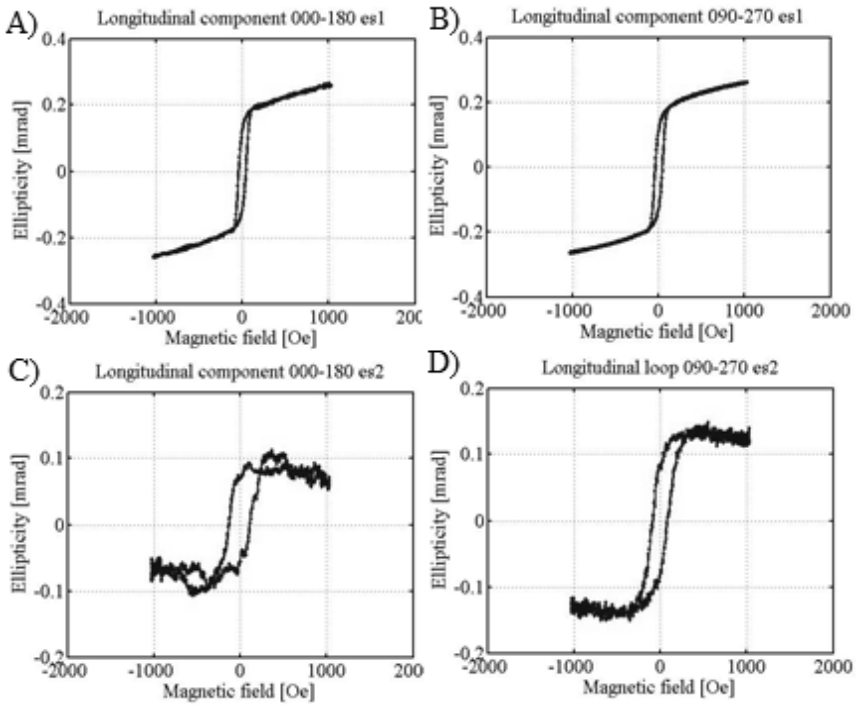

Fig 53: Comparison of longitudinal effects for the Kerr ellipticity for primary (A, B) and secondary (C, D) reflected beam at s-polarization.

At the second reflections, we register the same shape of the longitudinal components for all angles of rotation. No systematic changes are seen when looking at the longitudinal components as a function of the sample rotation. Their remnant magnetization remains the same at each angle of rotation and configuration, except the secondary reflections, where the remanent magnetization of longitudinal components of Kerr rotation and Kerr ellipticity is slightly larger after the rotation of 180°. This could indicate the small film or depth inhomogeneity of the sample which would be in accordance with ellipsometric measurements where the thickness inhomogeneity was investigated during the data fit to be about 10 %. Nevertheless, the results demonstrate that the sample does not show significant anisotropy.

MBE270515 – results – p-polarization

Figure 54 shows the original measured MO hysteresis loops of Kerr rotation and Kerr ellipticity measured at p-polarization for primary reflected laser beam. The hysteresis loops were measured at longitudinal configuration for 0° and 180 °.

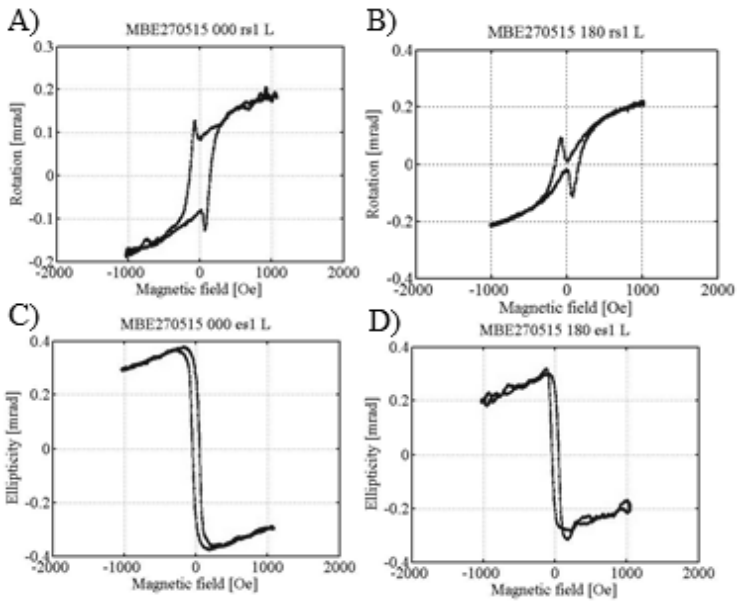

Fig. 54: Hysteresis loops - longitudinal configuration, p-polarization, A) Kerr rotation at 0°, B) Kerr rotation at 180°, C) Kerr ellipticity at 0°, D) Kerr ellipticity at 180°.

Figure 55 shows the original measured MO hysteresis loops at p-polarization for primary reflected laser beam measured at transversal configuration for 90° and 270°.

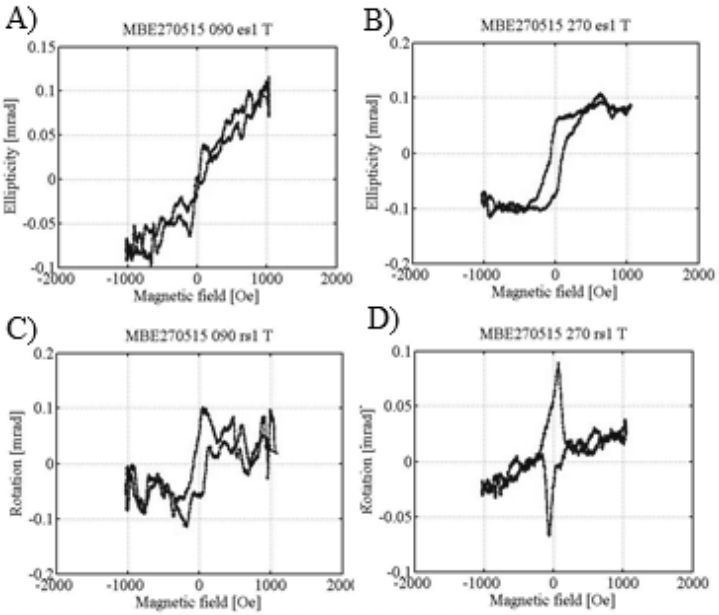

Fig. 55: Hysteresis loops - transversal configuration, p-polarization, A) Kerr rotation at 90°, B) Kerr rotation at 270°, C) Kerr ellipticity at 90°, D) Kerr ellipticity at 270°.

The shapes of the loops are slightly different which could again indicate the presence of polar contribution to the hysteresis loops. Figure 56 show separated magnetic components (using (9), (10)) for p-polarization and primary reflected laser beam.

polar component **longitudinal component** **transversal component**

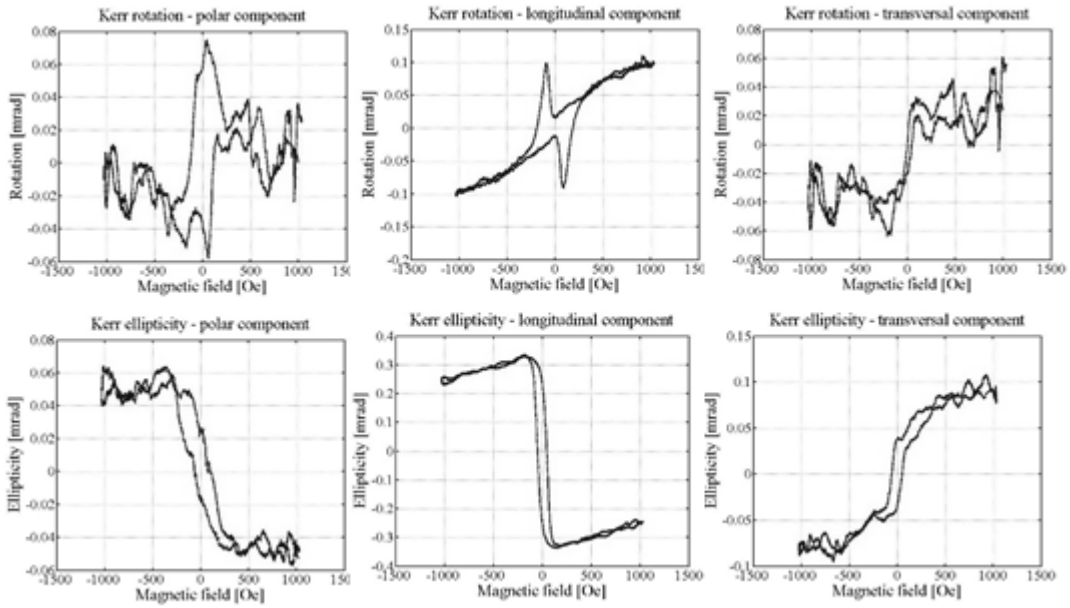

Fig. 56: Separated magnetic components for p-polarization, primary reflected laser beam. Polar, longitudinal and transversal component of Kerr rotation (upper row), and Kerr ellipticity (bottom row).

From the above separated magnetic components we can see that the results are similar to those at s-polarization. Except the difference in longitudinal components for the Kerr rotation and Kerr ellipticity, where in the Kerr rotation there are probably mixed different contributions of the magnetization.

The difference between the first and the second reflection is demonstrated on longitudinal effects shown below (Fig 57 and Fig. 58), where we study the dependence on the sample rotation (in-plane sample anisotropy). Longitudinal components were separated from the hysteresis loops measured at 0°, 90°, 180, and 270°.

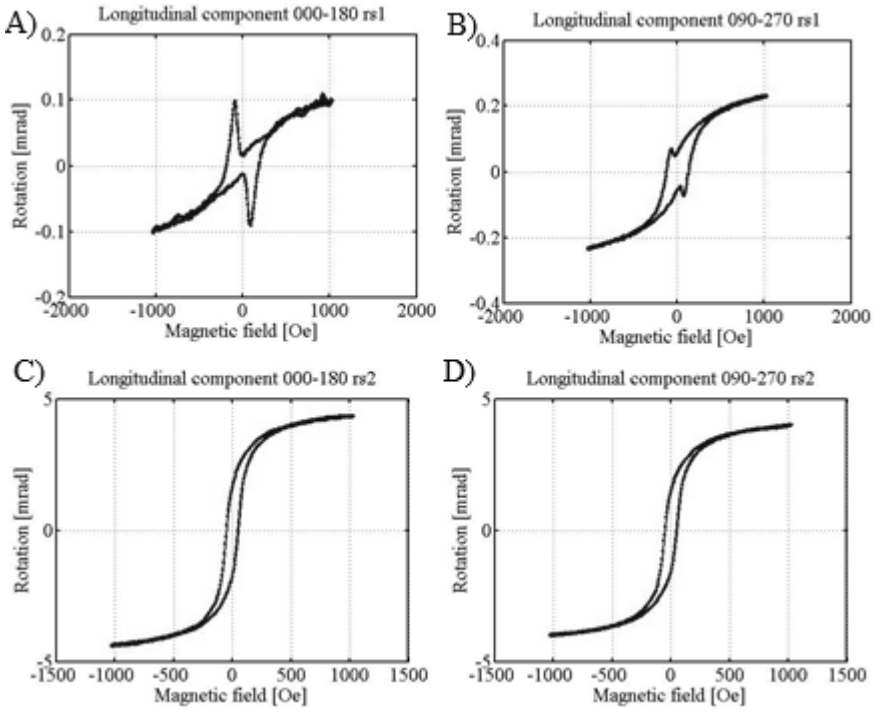

Fig. 57: Comparison of longitudinal effects for the Kerr rotation for primary (A, B) and secondary (C, D) reflected beam at p-polarization.

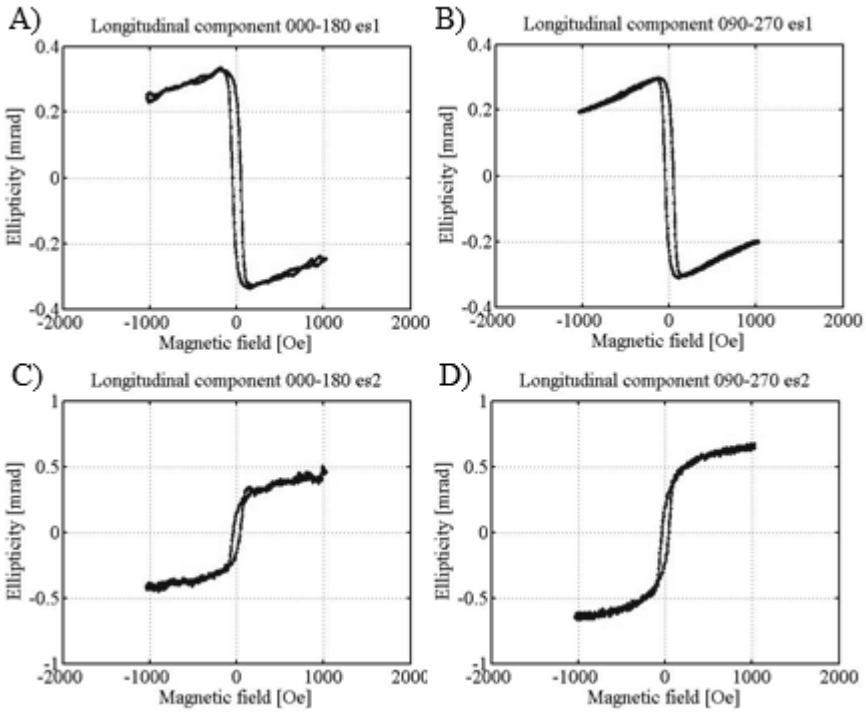

Fig 58: Comparison of longitudinal effects for the Kerr ellipticity for primary (A, B) and secondary (C, D) reflected beam at p-polarization.

At the second reflections, we register again the same shape of the longitudinal components for all angles of rotation and the longitudinal components as a function of the sample rotation show no systematic changes. Their remnant magnetization remains the same at each angle of rotation and configuration, except the secondary reflections, where the remanent magnetization of longitudinal components of Kerr rotation and Kerr ellipticity is slightly larger after the rotation of 180°. This could confirm the small film or depth inhomogeneity of the sample which could be also indicated by a small change in shape of the hysteresis loop showing longitudinal component of the Kerr rotation. Curvature of the loop is probably caused by a different contributions of magnetization of sublattices in the garnet structure and it is worth to study this phenomena further.

According to the results, the sample does not show significant anisotropy. Results indicate small thin film or depth inhomogeneity which was confirmed by ellipsometric measurements.

Separated contributions to magnetization

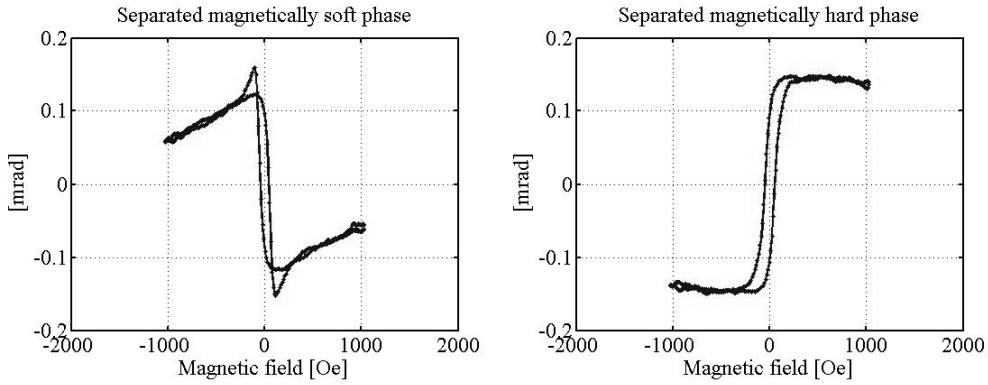

Fig. 59: Separated magnetization contributions for the sample MBE270515 from longitudinal hysteresis loops at p-polarization at the angle of rotation of 0° and 180°.

Magnetization contributions show different shapes whose origin will be investigated in future work. This results does not show yet whether they come from the different sublattices, different depth of the thin film, or grains on its surface.

MBE190616 – results – s-polarization

This sample was measured and analyzed exactly the same way as the previous one only with the difference in the electric current which was set to the value about 4.8 A. The results

for the polar and transversal components are comparable with respect to smaller overall size of the effects in this sample probably due to a different composition of thin film with smaller content of Bi. According to that, only the main results – the differences in longitudinal components for primary reflected beam– are shown. In Figure 60 we study the dependence on the sample rotation (in-plane sample anisotropy). Longitudinal components were separated from the hysteresis loops measured at 0°, 90°, 180, and 270°.

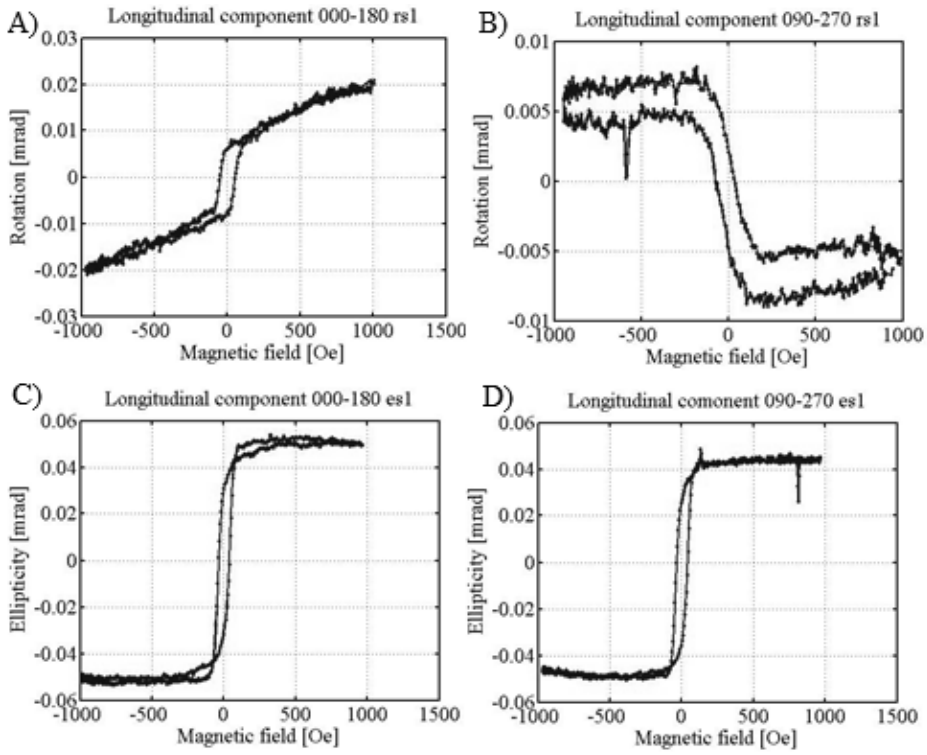

Fig. 60: Comparison of longitudinal magnetic components for s-polarization, primary reflected laser beam. A), B) shows Kerr rotation, and C), D) shows Kerr ellipticity.

According to the longitudinal components, the magnetization in the sample lies mainly in-plane. However, a small remanent polar component was present and decreased for higher external magnetic field. We register the same shape of the longitudinal components for all angles of rotation at the Kerr rotation configuration, and for ellipticity as well. No systematic changes are seen when looking at the longitudinal components as a function of the sample rotation. Their remnant magnetization remains the same at each angle of rotation. The difference between the shape of the hysteresis loops for Kerr rotation and Kerr ellipticity indicates small film or depth inhomogeneity of the sample which would be in accordance

with ellipsometric measurements where the thickness inhomogeneity was investigated during the data fit to be about 11 %. Nevertheless, the results demonstrate that the sample does not show significant anisotropy.

MBE190615 – results – p-polarization

Figure 61 shows longitudinal components separated from the hysteresis loops measured at 0°, 90°, 180, and 270°.

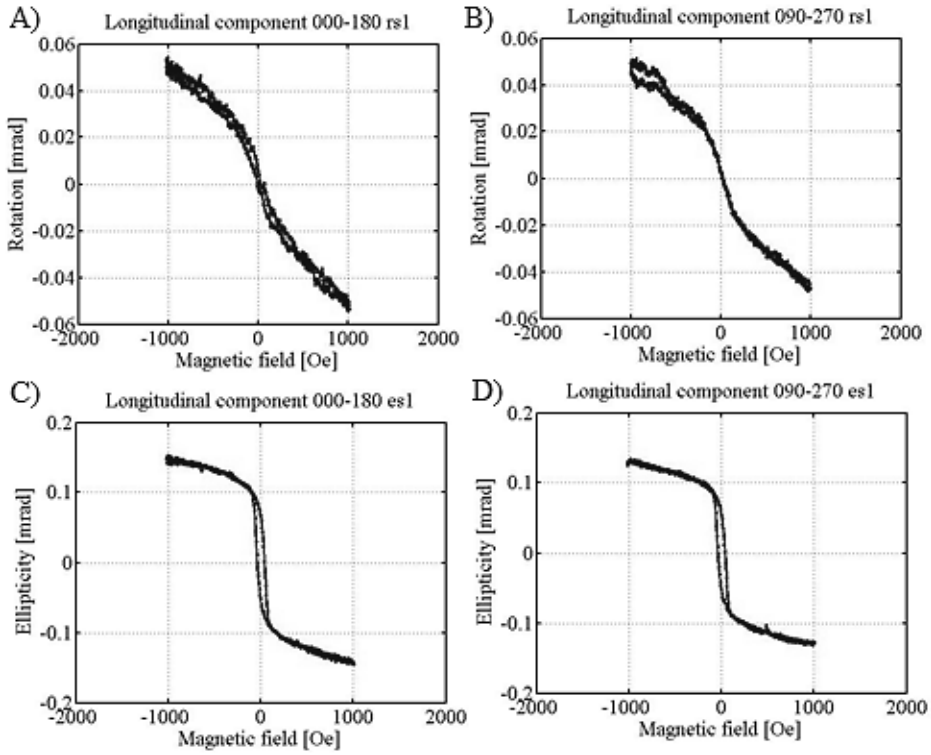

Fig. 61: Comparison of longitudinal magnetic components for p-polarization, primary reflected laser beam. A), B) shows Kerr rotation, and C), D) shows Kerr ellipticity.

We see no systematic changes of the remanent magnetization of longitudinal components. The difference between the shape of the hysteresis loops for Kerr rotation and Kerr ellipticity indicates again the small film or depth inhomogeneity. The results are similar to those at s-polarization except the difference in the shape of the Kerr rotation loops. The different contributions of the magnetization occur like in the sample MBE270515, but much weaker.

According to the results, the sample does not show anisotropy but indicate small thin film or depth inhomogeneity which was confirmed by ellipsometric measurements.

Separated contributions to magnetization

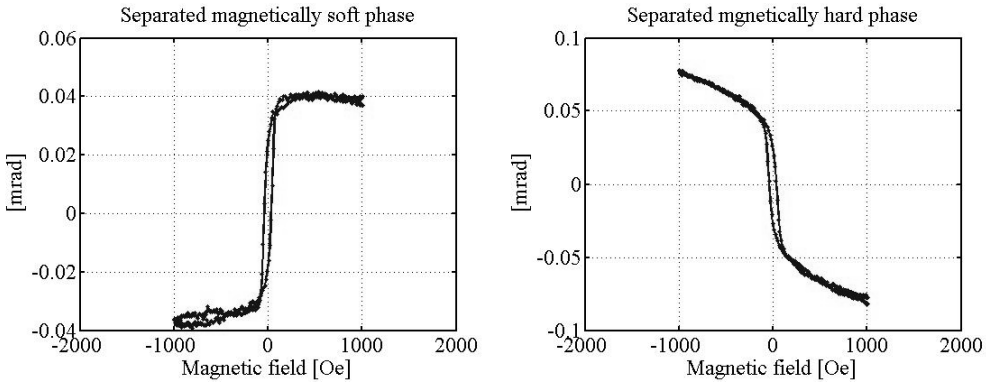

Fig. 62: Separated magnetization contributions for the sample MBE190615 from longitudinal hysteresis loops at p-polarization at the angle of rotation of 0° and 180°.

Magnetization contributions show very slight difference but again, we are not able to determine their origin.

4.10. Magneto-optical spectra

To contribute to the results from MOKE, the magneto-optical spectra measurements on an ellipsometric setup were performed. The angle of incidence of light was 45°. Subtraction of averaged measured data for opposite magnetization in both, longitudinal and transversal configuration led to the differential Mueller matrices showed in following figures (Figure 63 – Figure 66).

MO spectra – sample MBE190615

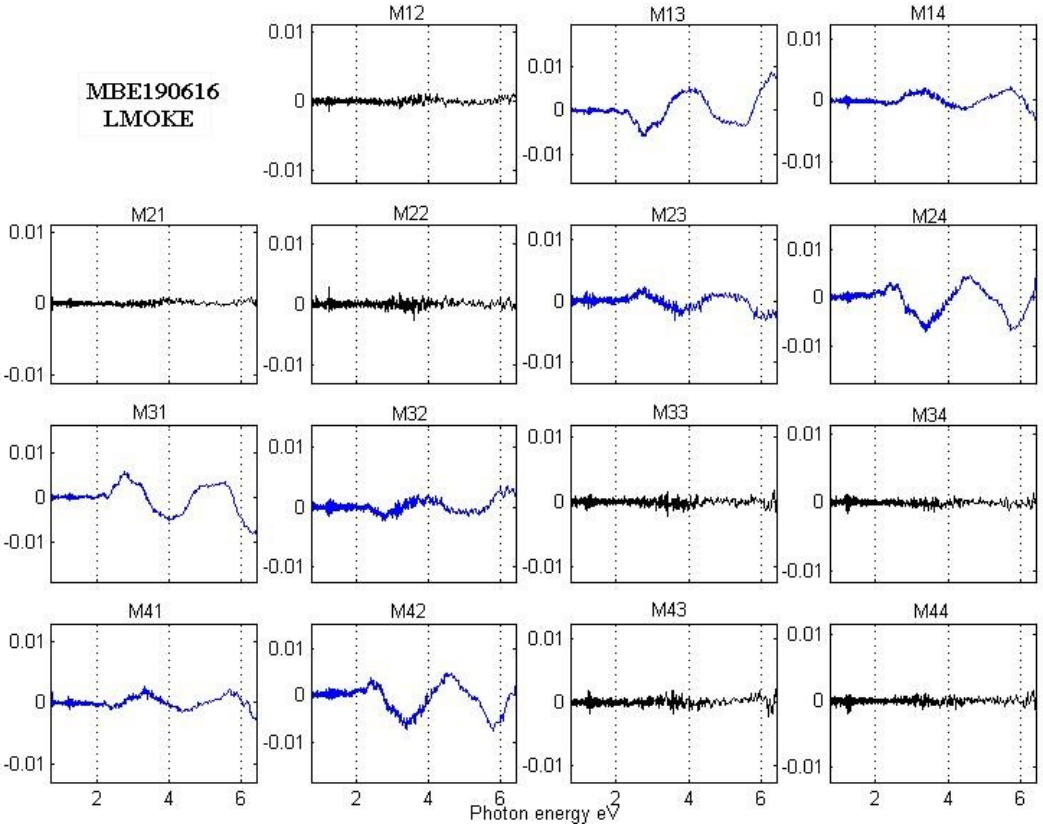

Fig. 63: Sample MBE190615: Measured differences from the Mueller matrix components obtained from MO measurements in longitudinal MO configuration (blue lines).

LMOKE response is detected in off-diagonal blocks of Mueller matrix. That corresponds to conversion between s- a p- polarization.

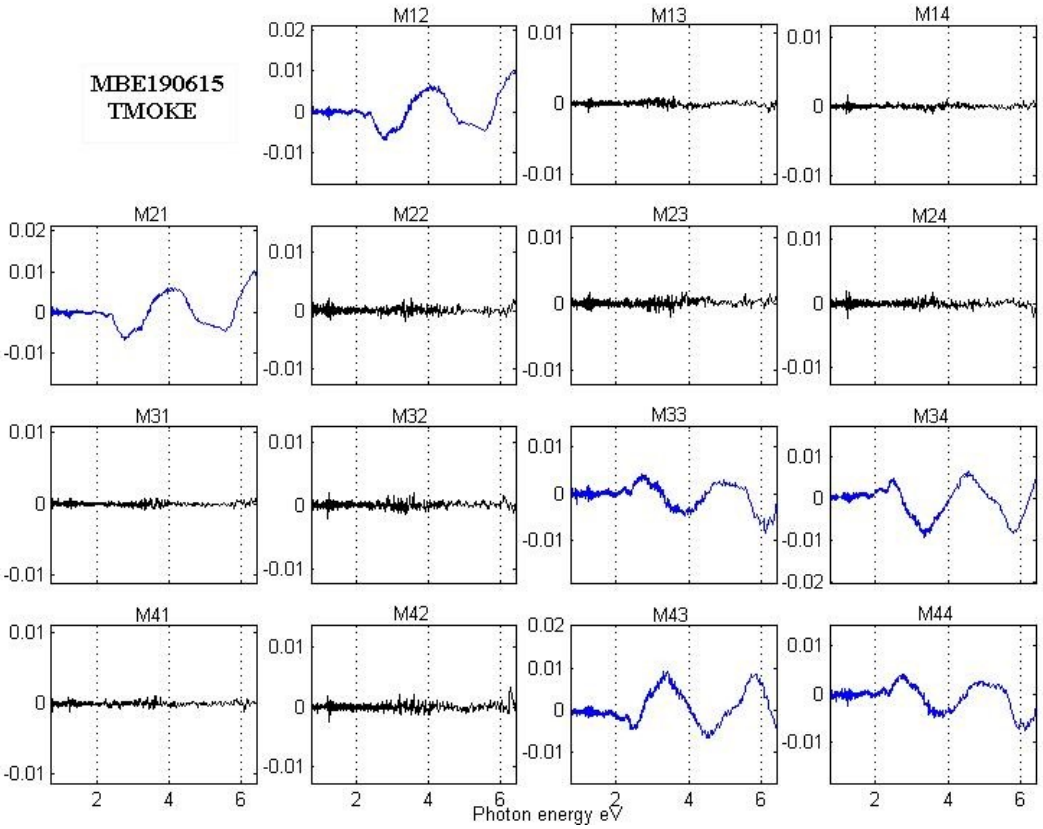

Fig. 64: Sample MBE190615Measured differences from the Mueller matrix components obtained from MO measurements in transverse MO configuration (blue lines).

TMOKE affects p-reflectivity and does not lead to a polarization conversion. Obtained block-diagonal matrix show occurrence of transversal effect.

MO spectra – sample MBE270515

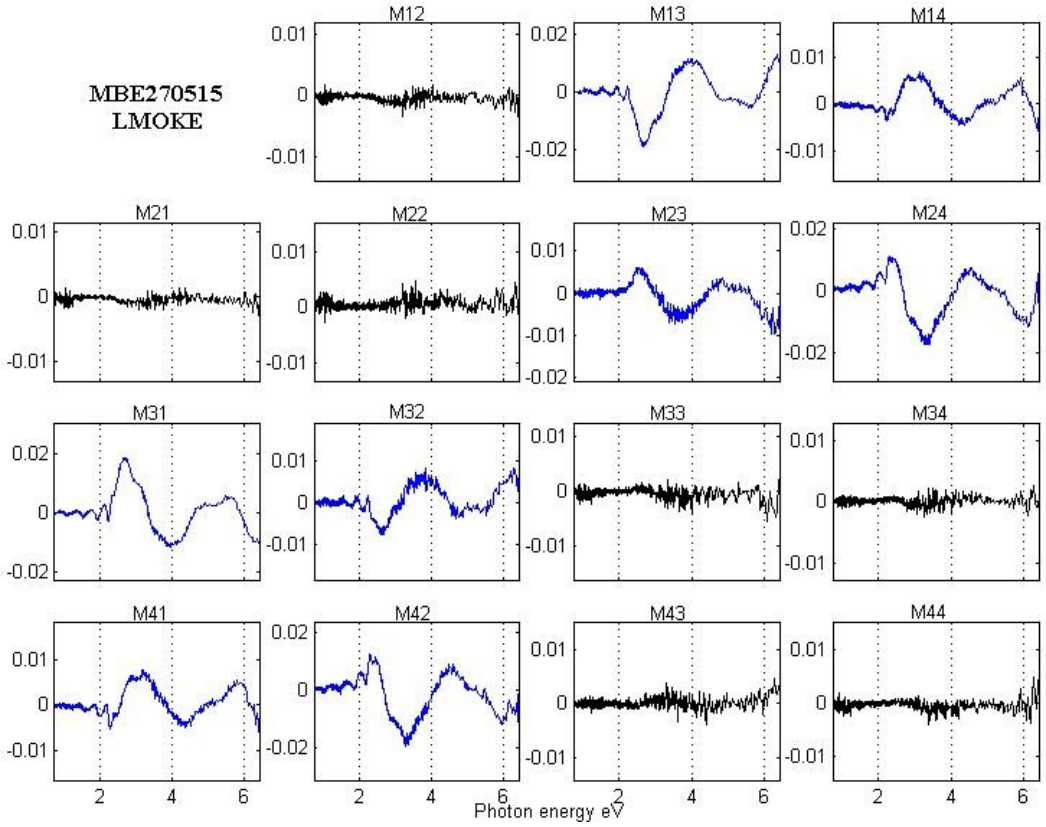

Fig. 65: Sample MBE270515Measured differences from the Mueller matrix components obtained from MO measurements in transverse MO configuration (blue lines).

Off-diagonal LMOKE Mueller matrix contains information about longitudinal and polar spectra together. In Figure 65 we can see longitudinal activity of the sample MBE270515. In all measurements, we can say that we had magnetic field big enough for saturation of this sample with higher Bi content.

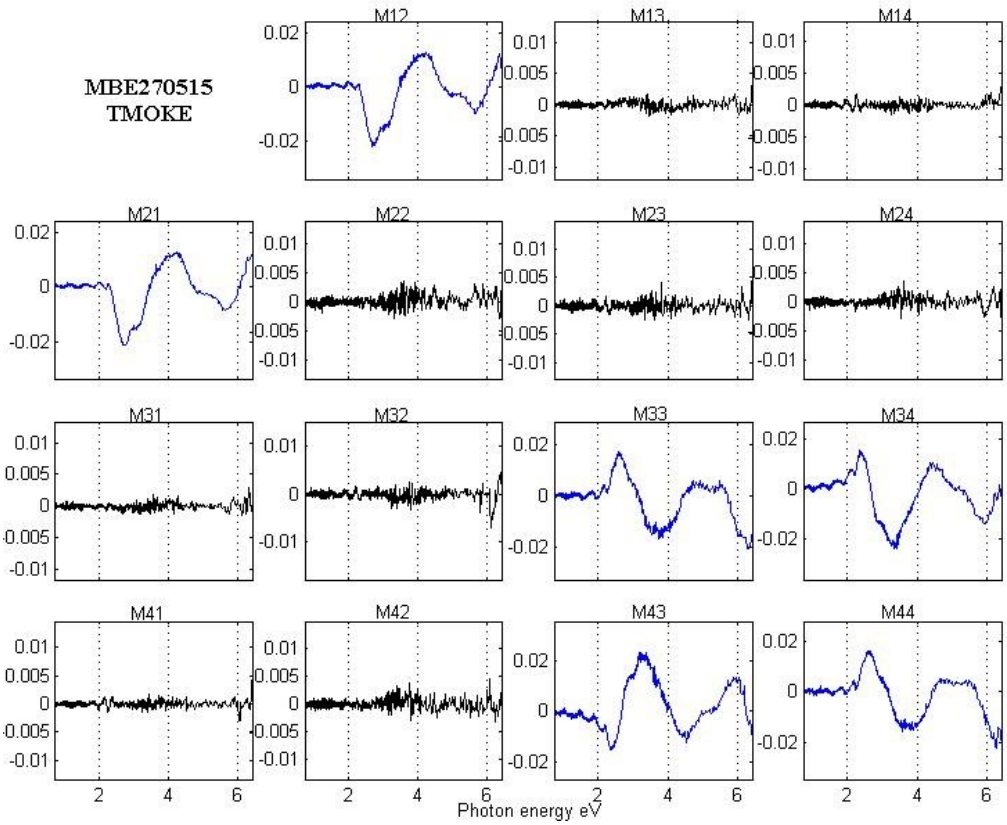

Fig. 66: Sample MBE270515: Measured differences from the Mueller matrix components obtained from MO measurements in longitudinal MO configuration (blue lines).

Block-diagonal Mueller matrix obtained in transversal configuration for sample MBE270515 show occurrence of slight tranversal activity, though higher than in previous sample.

LMOKE MO spectra measurements help to determine Kerr rotation and Kerr ellipticity of thin films. Using optical spectra measured at the same angle of incidence we can separate the tranversal effect, too. Data are usually compared with model to obtain spectral function of MO activity and thus comprehensive information about mageto-optical properties of the sample.

5. CONCLUSION AND FUTURE PERSPECTIVES

Two series of crystalline Bi:YIG thin films including targets for the deposition were successfully prepared by PLD technique varying only O2 pressure and substrate temperature as deposition conditions. At the beginning of each deposition, the conditions for depositing new Bi:YIG thin film on the GGG substrate were estimated based on knowledge from literature and conditions and the results of the previous deposition process of last deposited Bi:YIG thin film. The conditions were successfully determined, even though some of the depositions took place almost at the temperature limit of a deposition chamber (~ 900 °C). The targets were characterized by SEM, and all the samples were characterized by different techniques such as, AFM, XRD, RHEED, profilometry, ellipsometry, and magneto-optical measurements giving information about thin films' morphology, stoichiometry, chemical composition, as well as crystallization, optical and magneto-optical properties.

SEM analysis and Emission spectroscopy analysis provided information about the stoichiometry transfer from the target, through plasma, to the thin film, and helped us to understand the influence of the target's morphology on roughness of thin films. The analysis in 4.3. was helpful to understand the dependence of the stoichiometry transfer on the deposition conditions. SEM pictures in chapter 4.2 showed that Bi evaporated faster from the center of the target than from the edges, and it helped to analyze laser beam trace over the target.

Magneto-optical measurements in the Faraday configuration confirmed the linear dependence of the measured properties (Tc, θF, εF) on Bi content.

The magneto-optical vectorial magnetometry was used to separate polar, longitudinal and transversal components of magnetization in the samples and various magnetization contributions. Different magnetization contributions occurred in both, Kerr and Faraday, hysteresis loops. The contributions probably originated from different sublattices in the garnet structure or different layers in a depth of the material since the magnetic anisotropy was refuted by MOKE measurements at least for thick samples. On the other hand, they revealed slight inhomogeneity in the depth, as the separation of magnetization components showed. Thickness non-uniformity (depth inhomogeneity) was proven by both, ellipsometric measurements with corresponding data fits, and MOKE measurements.

Spectroscopic ellipsometry was used to determine optical constants and thickness of the layers. Polar MO spectra in the form of Mueller matrices were measured using the same ellipsometric set-up just with an additional in-plane magnet.

The MO spectra will help to determine Kerr rotation and Kerr ellipticity of thin films which is one of my future perspectives. Using optical spectra measured at the same angle of incidence I would like to separate the longitudinal, polar and transversal effect from MO spectra. As a future step, the obtained data will be compared with a model to obtain a spectral function of MO activity and thus comprehensive information about mageto-optical properties of the samples. The next perspective is to investigate the origin of different contributions to magnetization that occurred in the hysteresis loops, and possibly to discover how to separate or determine the magnetizations contribution of each sublattice.

REFERENCES

[1] CULLITY, B. and C. GRAHAM *Introduction to magnetic materials. 2nd ed. Hoboken*, N.J.: IEEE/Wiley, 2009. ISBN 978-047-1477-419.

[2] GALSTYAN, O. A. Dependence of Magneto-Optical Properties of Bi-YIG Thin Films on Post-Annealing Temperature. *Armenian Journal of Physics* [online]. 2015, **8**(1), 21-29 [cit. 2016-05-10]. ISSN 1829-1171.

[3] BERZHANSKY, V., A. SHAPOSHNIKOV, A. KARAVAINIKOV et al. The Effect of Faraday Rotation Enhancement in Nanolayered Structures of Bi - Substituted Iron Garnets. *Solid State Phenomena* [online]. 2013, **200**, 233-238 [cit. 2016-05-10]. DOI: 10.4028/www.scientific.net/SSP.200.233. ISSN 1662-9779. Dostupné z: http://www.scientific.net/SSP.200.233

[4] SHAPOSHNIKOV, A. N., A. R. PROKOPOV, A. V. KARAVAINIKOV et al. Modification of Bi:YIG film properties by substrate surface ion pre-treatment. *Materials Research Bulletin* [online]. 2014, **55**, 19-25 [cit. 2016-05-10]. DOI:

10.1016/j.materresbull.2014.03.035. ISSN 00255408. Available from : http://linkinghub.elsevier.com/retrieve/pii/S0025540814001718

[5] CHERN, M.-Y., F.-Y. LO, D.-R. LIU, K. YANG and J.-S. LIAW. Red Shift of Faraday Rotation in Thin Films of Completely Bismuth-Substituted Iron Garnet Bi 3 Fe 5 O 12. *Japanese Journal of Applied Physics* [online]. 1999, **38**(112), 6687-6689 [cit. 2016-05-10]. DOI: 10.1143/JJAP.38.6687. ISSN 0021-4922. Available from: http://stacks.iop.org/1347-4065/38/6687

[6] POPOVA, E., L. MAGDENKO, H. NIEDOBA et al.. Magnetic properties of the magnetophotonic crystal based on bismuth iron garnet. *Journal of Applied Physics* [online]. 2012, **112**(9), 093910- [cit. 2016-05-10]. DOI: 10.1063/1.4764345. ISSN 00218979. Available from: http://scitation.aip.org/content/aip/journal/jap/112/9/10.1063/1.4764345

[7] NUR-E-ALAM, M., M. VASILIEV, K. ALAMEH, V. KOTOV, V. DEMIDOV and D. BALABANOV. YIG:Bi_2O_3 Nanocomposite Thin Films for Magnetooptic and Microwave Applications. *Journal of Nanomaterials* [online]. 2015, **2015**, 1-6 [cit. 2016-05-10]. DOI: 10.1155/2015/182691. ISSN 1687-4110. Available from: http://www.hindawi.com/journals/jnm/2015/182691/

[8] YANG, Q., H. ZHANG and Y. LIU. Study of magnetic and magneto-optical properties of heavily doped bismuth substitute yttrium iron garnet (Bi: YIG) film. *Rare Metals* [online]. 2006, **25**(6), 557-561 [cit. 2016-05-10]. DOI: 10.1016/S1001-0521(07)60145-4. ISSN 10010521. Available from: http://linkinghub.elsevier.com/retrieve/pii/S1001052107601454

[9] EDITED BY HUANG HUNG-CHIA, A. *Optical Waveguide Sciences Proceedings of the International Symposium, held at Kweilin, People's Republic of China (PRC), June 20-23, 1983*. 1. Dordrecht: Springer Netherlands, 1983, 360 s. ISBN 978-940-0968-752.

[10] HAYASHI, H., S. IWASA, N. VASA et al. Fabrication of Bi-doped YIG optical thin film for electric current sensor by pulsed laser deposition. *Applied Surface Science* [online]. 2002, **197-198**, 463-466 [cit. 2016-05-11]. DOI: 10.1016/S0169-

4332(02)00364-1. ISSN 01694332. Available from: http://linkinghub.elsevier.com/retrieve/pii/S0169433202003641

[11] BOUDIAR, T., B. PAYET-GERVY, M.-F. BLANC-MIGNON, J.-J. ROUSSEAU, M. LE BERRE and H. JOISTEN. Magneto-optical properties of yttrium iron garnet (YIG) thin films elaborated by radio frequency sputtering. *Journal of Magnetism and Magnetic Materials* [online]. 2004, **284**, 77-85 [cit. 2016-05-10]. DOI: 10.1016/j.jmmm.2004.06.046. ISSN 03048853. Available from: http://linkinghub.elsevier.com/retrieve/pii/S0304885304006845

[12] ELDADA, L. Integrated optics need magnets. In: *EE Times* [online]. Wilmington, Mass.: Telephotonics Inc., 2001 [cit. 2016-05-11]. Available from: http://www.eetimes.com/document.asp?doc_id=1204221

[13] SIEGEL, G., M. PRESTGARD, S. TENG and A. TIWARI. Robust longitudinal spin-Seebeck effect in Bi-YIG thin films. *Scientific Reports* [online]. 2014, **4**, - [cit. 2016-05-10]. DOI: 10.1038/srep04429. ISSN 2045-2322. Available from: http://www.nature.com/articles/srep04429

[14] SIEGEL, G., M. PRESTGARD, H. YANG and A. TIWARI. Spin Current Response in Bi-YIG/Pt Thin Film Heterostructures Induced by Gamma Radiation. *IEEE Electron Device Letters* [online]. 2015, **36**(8), 853-855 [cit. 2016-05-10]. DOI: 10.1109/LED.2015.2449337. ISSN 0741-3106. Available from: http://ieeexplore.ieee.org/lpdocs/epic03/wrapper.htm?arnumber=7132727

[15] GALSTYAN, O., H. LEE, J. PARK, Y. LEE, K. LEE*, A. BABAJANYAN and D. CHA. Magneto-optical Imaging Using $Bi_2Y_1Fe_5O_{12}$ Thin Films Prepared on Glass Substrates by Using the MOD Method. *New Physics: Sae Mulli* [online]. 2014, **64**(11), 1089-1092 [cit. 2016-05-10]. DOI: 10.3938/NPSM.64.1089. ISSN 0374-4914. Available from: http://www.npsm-kps.org/journal/DOIx.php?id=10.3938/NPSM.64.1089

[16] LAULAJAINEN, M., P. PATURI, J. RAITTILA, H. HUHTINEN, A. B. ABRAHAMSEN, N. H. ANDERSEN and R. LAIHO. BixY3−xFe5O12 thin films prepared by laser ablation for magneto-optical imaging of superconducting thin films. *Journal of Magnetism and Magnetic Materials* [online]. 2004, **279**(2-3), 218-223 [cit.

2016-05-11]. DOI: 10.1016/j.jmmm.2004.01.081. ISSN 03048853. Available from: http://linkinghub.elsevier.com/retrieve/pii/S0304885304001830

[17] GALSTYAN, O., H. LEE, A. BABAJANYAN, A. HAKHOUMIAN, B. FRIEDMAN and K. LEE. Magneto-optical visualization by Bi: YIG thin films prepared at low temperatures. *Journal of Applied Physics* [online]. 2015, **117**(16), 163914- [cit. 2016-05-13]. DOI: 10.1063/1.4918907. ISSN 0021-8979. Available from: http://scitation.aip.org/content/aip/journal/jap/117/16/10.1063/1.4918907

[18] CHAKRAVARTY, A. *Geometry Induced Magneto-optic Effects in PLE Magnetic Garnet Films*. Houghton, USA, 2015. Dissertation. Michigan Technological University.

[19] EDITED BY E. P. WOHLFARTH. VOL. 2., *Ferromagnetic materials: a handbook on the properties of magnetically ordered substances* [online]. Repr. Amsterdam: North-Holland, 1982 [cit. 2016-05-10]. ISBN 978-044-4853-127.

[20] VERTRUYEN, B., R. CLOOTS, J. ABELL, T. JACKSON, R. DA SILVA, E. POPOVA and N. KELLER Curie temperature, exchange integrals, and magneto-optical properties in off-stoichiometric bismuth iron garnet epitaxial films. *Physical Review B* [online]. 2008, **78**(9), - [cit. 2016-05-10]. DOI: 10.1103/PhysRevB.78.094429. ISSN 1098-0121. Available from: http://link.aps.org/doi/10.1103/PhysRevB.78.094429

[21] EDITED BY BEKIR AKTAS and F. MIKAILOV., *Advances in nanoscale magnetism proceedings of the International Conference on Nanoscale Magnetism*. [Online-Ausg.].122. Berlin: Springer, 2008, 330 s. ISBN 35-406-9882-5.

[22] DAVIDENKO, I., M. FALLY and R. RUPP. Magnetic and optical anisotropy in garnets induced by spatially modulated elliptically polarized light. *Journal of Magnetism and Magnetic Materials* [online]. 2001, **226-230**(55), 958-960 [cit. 2016-05-10]. DOI: 10.1016/S0304-8853(00)01310-X. ISSN 03048853. Available from: http://linkinghub.elsevier.com/retrieve/pii/S030488530001310X

[23] KORONOVSKYY, V. and A. KALENICHENKO. Electromagneto-Optical Scanning of the Magnetic Domains Local Areas of Bismuth-Substituted Yttrium Iron

Garnets. *Journal of Modern Physics* [online]. 2011, **02**(08), 908-912 [cit. 2016-05-10]. DOI: 10.4236/jmp.2011.28107. ISSN 2153-1196. Available from: http://www.scirp.org/journal/PaperDownload.aspx?DOI=10.4236/jmp.2011.28107

[24] VEIS, M., E. LIŠKOVÁ, R. ANTOŠ et al. Polar and longitudinal magneto-optical spectroscopy of bismuth substituted yttrium iron garnet films grown by pulsed laser deposition. *Thin Solid Films* [online]. 2011, **519**(22), 8041-8046 [cit. 2016-05-10]. DOI: 10.1016/j.tsf.2011.06.007. ISSN 00406090. Available from: http://linkinghub.elsevier.com/retrieve/pii/S0040609011012636

[25] LEE, H., Y. YOON, S. KIM et al. Preparation of bismuth substituted yttrium iron garnet powder and thin film by the metal-organic decomposition method. *Journal of Crystal Growth* [online]. 2011, **329**(1), 27-32 [cit. 2016-05-10]. DOI: 10.1016/j.jcrysgro.2011.06.048. ISSN 00220248. Available from: http://linkinghub.elsevier.com/retrieve/pii/S0022024811005756

[26] BERZHANSKY, V., T. MIKHAILOVA, A. SHAPOSHNIKOV, A. PROKOPOV, A. KARAVAINIKOV, V. KOTOV, D. BALABANOV and V. BURKOV. Magneto-optics of nanoscale Bi:YIG films. *Applied Optics* [online]. 2013, **52**(26), 6599-6606 [cit. 2016-05-12]. DOI: 10.1364/AO.52.006599. ISSN 0003-6935. Available from: https://www.osapublishing.org/abstract.cfm?URI=ao-52-26-6599

[27] BI, L., J. HU, P. JIANG, H. KIM, D. KIM, M. ONBASLI, G. DIONNE and C. ROSS. Magneto-Optical Thin Films for On-Chip Monolithic Integration of Non-Reciprocal Photonic Devices. *Materials* [online]. 2013, **6**(11), 5094-5117 [cit. 2016-05-12]. DOI: 10.3390/ma6115094. ISSN 1996-1944. Available from: http://www.mdpi.com/1996-1944/6/11/5094/

[28] BLOCK, A., P. DULAL, B. STADLER and N. SEATON. Growth Parameters of Fully Crystallized YIG, Bi:YIG, and Ce. *IEEE Photonics Journal* [online]. 2014, **6**(1), 1-8 [cit. 2016-05-10]. DOI: 10.1109/JPHOT.2013.2293610. ISSN 1943-0655. Available from: http://ieeexplore.ieee.org/lpdocs/epic03/wrapper.htm?arnumber=6678201

[29] DOORMANN, V., J.-P. KRUMME and H. LENZ. Optical and magneto-optical tensor spectra of bismuth-substituted yttrium-iron-garnet films. *Journal of Applied*

Physics [online]. 1990, **68**(7), 3544-3553 [cit. 2016-05-12]. DOI: 10.1063/1.346314. ISSN 00218979. Available from: http://scitation.aip.org/content/aip/journal/jap/68/7/10.1063/1.346314

[30] HAYAKAWA, E., T. NAMIKAWA and Y. YAMAZAKI. Effects of Annealing Atmosphere on Magnetooptical Properties of Sputtered Bi-Substituted Garnet Films. *IEEE Translation Journal on Magnetics in Japan* [online]. 1988, **3**(6), 487-488 [cit. 2016-05-13]. DOI: 10.1109/TJMJ.1988.4563753. ISSN 0882-4959. Available from: http://ieeexplore.ieee.org/lpdocs/epic03/wrapper.htm?arnumber=4563753

[31] MARTYNKOVÁ, G. S., M. RUEMMELI and K. ČECH BARABASZOVÁ. *Introduction to nanocomposite science of layered and tubular materials*. Hauppauge, N.Y.: Nova Science Publishers, 2012. ISBN 978-160-7417-392.

[32] OHRING, M. *Materials science of thin films: deposition and structure*. 2nd ed. San Diego, CA: Academic Press, 2002. ISBN 01-252-4975-6.

[33] WANG, K. Laser Based Fabrication of Graphene. *Advances in Graphene Science* [online]. InTech, 2013 [cit. 2016-05-13]. DOI: 10.5772/55821. ISBN 978-953-51-1182-5. Available from: http://www.intechopen.com/books/advances-in-graphene-science/laser-based-fabrication-of-graphene

[34] ŠAFÁŘOVÁ, K. *Skenovací (rastrovací) elektronová mikroskopie.* Workshop: Mikroskopické techniky SEM a TEM. Centrum pro výzkum nanomateriálů, Olomouc., 2012. Available from: http://nanosystemy.upol.cz/upload/18/safarova_sem.pdf

[35] KOPECKÁ, J. *Elektronová mikroskopie*. Učební text. Laboratoř charakterizace nano a mikrosystémů, VŠCHT v Praze., 2014.

[36] ECKERTOVÁ, L. *Physics of thin films*. 2nd rev. ed. New York: Plenum Press, 1986. ISBN 03-064-1798-7.

[37] GALBÁCS, G. *Atomic Spectroscopy*. Presentation. University of Szeged, Szeged, 2016. Available from: http://www2.sci.u-szeged.hu/inorg/Physical%20analysis%202010%20-%20Atomic%20spectroscopy%20and%20automatic%20analyzers.pdf

[38] Definition of Atomic-emission spectroscopy (AES, OES). *Chemicool* [online]. 2016 [cit. 2016-05-13]. Available from: http://www.chemicool.com/definition/atomic_emission_spectroscopy_aes_oes.html

[39] MAMULOVÁ KUTLÁKOVÁ, K. *Krystalová struktura a rentgenová difrakce*. Učební text. Vysoká škola báňská – Technická univerzita Ostrava, Ostrava, 2013.

[40] MATĚJKA, V. *AFM a SPM.* Učební text. Vysoká škola báňská – Technická univerzita Ostrava, Ostrava, 2014.

[41] Optical Profilometry: How a Profilometer Works. In: *Nano Science instruments* [online]. Washington, DC: Nano Science instruments, 2016 [cit. 2016-05-12]. Available from: http://www.nanoscience.com/technology/optical-profiler-technology/how-profilometer-works/

[42] KUNČICKÁ, Š. *Color Effects in Optical Spectroscopy*. Ostrava, 2014. Bachelor thesis. VŠB – Technical University of Ostrava, University Study Programmes, Institute of Physics.

[43] POPIOLEK-MASAJADA, A., W. URBANCZYK, K. POSTAVA, L. HALAGAČKA, M. VANWOLLEGHEM and J. PIŠTORA *Magneto-optics: from bulk materials to nanostructures* [online]. b.r., , 94411 [cit. 2016-05-12]. DOI: 10.1117/12.2176299. Available from: http://proceedings.spiedigitallibrary.org/proceeding.aspx?doi=10.1117/12.2176299

[44] POSTAVA, K., J. HAMRLE, J. HAMRLOVÁ, D. HRABOVSKÝ, O. ŽIVOTSKÝ, N.A. IVOTSKŠ, J. PIŠTORA and D. LUKÁŠ. Depth and material sensitivity in magneto-optic nanostructures. *International Journal of Nanotechnology* [online]. 2012, **9**(8-9), 784-808 [cit. 2016-05-12]. DOI: 10.1504/IJNT.2012.046753. ISSN 1475-7435. Available from: http://www.inderscience.com/link.php?id=46753

[45] SAIDL, V. *Studium magneticky uspořádaných materiálů pomocí optické spektroskopie*. Praha, 2013. Diplomová práce. Univerzita Karlova v Praze, Matematicko-fyzikální fakulta.

[46] DABOO, C, J. BLAND, R. HICKEN, A. IVES, M. BAIRD and M. WALKER. Vectorial magnetometry with the magneto-optic Kerr effect applied to Co/Cu/Co trilayer structures. *Physical Review B. Condensed Matter*. 1993, **47**(18), 11852-11859.

[47] DING, H., S. PUTTER, H. OEPEN and J. KIRSCHNER. Experimental method for separating longitudinal and polar Kerr signals. *Journal of Magnetism and Magnetic Materials*. 2000, **212**(1-2), 5-11.

[48] POSTAVA, K., D. HRABOVSKÝ, J. HAMRLOVÁ, J. PIŠTORA, A. WAWRO, L.T. BACZEWSKI, I. SVEKLO and A. MAZIEWSKI. Selective sensitivity of ellipsometry to magnetic nanostructures. *Thin Solid Films* [online]. 2011, **519**(9), 2627-2632 [cit. 2016-05-13]. DOI: 10.1016/j.tsf.2010.11.073. ISSN 00406090. Available from: http://linkinghub.elsevier.com/retrieve/pii/S0040609010016196

[49] HALAGAČKA, L., K. POSTAVA, M. VANWOLLEGHEM, F. VAURETTE, J. BEN YOUSSEF, B. DAGENS and J. PIŠTORA. *Mueller matrix optical and magneto-optical characterization of Bi-substituted gadolinium iron garnet for application in magnetoplasmonic structures* [online]. b.r. [cit. 2016-05-14]. DOI: 10.1364/OME.4.001903. Available from: https://www.osapublishing.org/ome/abstract.cfm?uri=ome-4-9-1903

[50] JOHS, B. and J. HALE. Dielectric function representation by B-splines. *Physica status solidi (a)* [online]. 2008, **205**(4), 715-719 [cit. 2016-05-13]. DOI: 10.1002/pssa.200777754. ISSN 18626300. Available from: http://doi.wiley.com/10.1002/pssa.200777754